The pole position of the $a_1(1260)$ resonance in a three-body unitary framework

Daniel Sadasivan,[1, *] Andrei Alexandru,[2, 3, †] Hakan Akdag,[4, ‡] Felipe Amorim,[1]
Ruairí Brett,[2, §] Chris Culver,[5, ¶] Michael Döring,[2, 6, **] Frank X. Lee,[2, ††] and Maxim Mai[2, ‡‡]

[1] *Ave Maria University, Ave Maria, FL 34142, USA*
[2] *The George Washington University, Washington, DC 20052, USA*
[3] *Department of Physics, University of Maryland, College Park, MD 20742, USA*
[4] *Helmholtz-Institut für Strahlen- und Kernphysik (Theorie) and Bethe*
Center for Theoretical Physics, Universität Bonn, 53115 Bonn, Germany
[5] *Department of Mathematical Sciences, University of Liverpool, Liverpool L69 7ZL, United Kingdom*
[6] *Thomas Jefferson National Accelerator Facility, Newport News, VA 23606, USA*

Masses, widths, and branching ratios of hadronic resonances are quantified by their pole positions and residues with respect to transition amplitudes on the Riemann sheets of the complex energy-plane. In this study we discuss the analytic structure in the physical energy region of three-body scattering amplitudes on such manifolds. As an application, we determine the pole position of the $a_1(1260)$ meson from the ALEPH experiment by allowing for $\pi\rho$ coupled channels in S and D wave. We find it to be $\sqrt{s_0} = (1232^{+15+9}_{-0.2-11} - i266^{+0.3+15}_{-22-27})$ MeV

I. INTRODUCTION

Hadronic resonances often decay strongly into three particles. Especially in the meson sector, three-body decays can be the dominant modes, e.g., for axial mesons like the $a_1(1260)$ [1]. Excited mesons are searched for in recent experimental efforts like GlueX [2], COMPASS [3], and at the BESIII accelerator [4] often in connection with exotic states that cannot consist of two constituent quarks only. For example, an exotic $\pi_1(1600)$ was found by COMPASS [3] in three-pion decays. These experiments entail new partial-wave analysis (PWA) efforts, e.g., by COMPASS [5, 6], BESIII [7, 8], CLEO [9], or in coupled channels using the PAWIAN framework for $p\bar{p}$ induced meson production [10].

On the theory side, the final state interaction of three strongly interacting particles has been studied with Khuri-Treiman equations and similar frameworks by the Bonn group, JPAC, and others for light meson decays [11–33]. Faddeev-type arrangements of chiral two-body amplitudes were used to predict resonance states and study known ones [34–38]. See also Ref. [39] for a pedagogical introduction into dispersive methods and Ref. [40] for connections between Khuri-Treiman equations and three-body unitary methods.

One such method applies the principle of three-body unitarity to construct three-to-three amplitudes [41] extending earlier work [42, 43] to the above-threshold regime. The subthreshold behavior of this amplitude has been studied in Refs. [29, 44] and new insights into covariant vs. time-ordered formulations for the interaction kernel were obtained recently [45]. The amplitude of Ref. [41] has been extended to formulate three-body resonance decays including a fit to the $a_1(1260) \to 3\pi$ lineshape and prediction of Dalitz plots [46]. This study is the basis of the current work.

Experimentally, the $a_1(1260)$ resonance can be produced in τ-decays [9, 47] via $\tau \to (3\pi)\nu_\tau$. Therefore, its three-pion dynamics can be separated off the weak primordial interaction to be measured cleanly for the $I^G(J^{PC}) = 1^-(1^{++})$ quantum numbers. This distinguishes this semileptonic τ decay from some of the aforementioned experiments in which multiple partial waves contribute to the final three-pion state. Of course, the a_1 resonance still couples to various configurations of the 2+1 pions, dominated by $\rho\pi$ in S-wave and $\sigma\pi$ in P-wave (σ standing for the $f_0(500)$ resonance), but also several smaller waves, see CLEO [9], COMPASS [5], and BESIII results [7]. Recent calculations based on chiral unitary methods predict that the $a_1(1260) \to \pi\sigma$ decay ratio is very small, in the few percent range [48]. This is in contrast to an older phenomenological study [9] finding a more substantial $\pi\sigma$ branching ratio. This shows that, despite the clean experimental way to produce the $a_1(1260)$, its properties such as branching fractions are under continued debate. The resonance is very wide (with very large uncertainties quoted by the PDG [1]), indicating strong and non-trivial three-body effects which makes it a prime candidate to study few-body dynamics. This is reflected in an increased interest in the properties and structure of the $a_1(1260)$ [46, 49–62], as well as the related τ-decay [63–68].

The study of the $a_1(1260)$ with the *ab-initio* techniques of lattice QCD has also made significant progress. For a pioneering calculation see Ref. [69] where the ρ-meson was treated as a stable particle, motivated by the small box size. Recently, this approximation was lifted by using up to three pion operators in combination with the finite-volume unitarity (FVU) three-body quantization

* daniel.sadasivan@avemaria.edu
† aalexan@gwu.edu
‡ akdag@hiskp.uni-bonn.de
§ rbrett@gwu.edu
¶ C.Culver@liverpool.ac.uk
** doring@gwu.edu
†† fxlee@gwu.edu
‡‡ maximmai@gwu.edu

condition [70, 71] that allowed for the first pole extraction of a three-body resonance from lattice QCD [72]. The infinite-volume version of that formalism is very similar to the one of Ref. [46] featuring coupled channels and explicit sub-channel (ρ) dynamics. See Refs. [73–75] for reviews on recent progress of three-body physics in lattice QCD.

In this work, we use the formalism of Ref. [72] to determine the $a_1(1260)$ pole position from experiment including statistical and some systematic uncertainties. This work is related to older determinations of the a_1 pole position [49] but also to Ref. [60] (JPAC), in which the S-wave $\rho\pi$ channel was used to fit the a_1 lineshape [47] with an approximately unitary formalism. In contrast, our formalism is manifestly unitary, which considerably complicates the analytic structure through the pertinent pion exchange mechanism and requires a thorough discussion in Sec. III based on the formalism summarized in Sec. II. As such, it provides the only pole determination in three-body unitary amplitudes except for Ref. [56] and Ref. [72]. However, in Ref. [56] the PDG pole position of the a_1 was fitted, while in this study we directly fit the lineshape from experiment. We therefore expect to extract the most reliable pole position of the $a_1(1260)$ resonance to date, with our results discussed in Sec. IV.

II. FORMALISM

The $a_1(1260)$ couples to three-pion states in the $I^G(J^{PC}) = 1^-(1^{++})$ channel that can be decomposed as $\pi\rho$ in S/D-wave, $\pi\sigma$ and $\pi(\pi\pi)_{I=2}$ in P-waves and other channels. Phenomenologically $(\pi\rho)_S$ is dominant [76] with the branching ratios into other channels quite uncertain [1], see also Ref. [48]. Therefore, we limit here the channel space to $\pi\rho$ in S and D waves. Finally, we note that the isobar formulation of the two-body subchannel dynamics used in this study is not an approximation but a re-parametrization of the full two-body amplitude [77, 78].

Our formalism from Ref. [46] is summarized in the following. The a_1 lineshape with $\pi^-\pi^-\pi^+$ final states,

$$
\mathcal{L}(\sqrt{s}) = N(m_\tau^2 - s)^2 \int \frac{\mathrm{d}^3 \boldsymbol{q}_1}{(2\pi)^3} \frac{\mathrm{d}^3 \boldsymbol{q}_2}{(2\pi)^3} \frac{\mathrm{d}^3 \boldsymbol{q}_3}{(2\pi)^3} \frac{(2\pi)^4}{8E_{q_1} E_{q_2} E_{q_3}}
$$
$$
\times \, \delta^4(P_3 - q_1 - q_2 - q_3)
$$
$$
\times \left(\Big| \sum_\lambda \hat{\Gamma}_{-1\lambda} \Big|^2 + \frac{m_\tau^2}{s} \Big| \sum_\lambda \hat{\Gamma}_{0\lambda} \Big|^2 + \Big| \sum_\lambda \hat{\Gamma}_{+1\lambda} \Big|^2 \right) \quad (1)
$$

depends on the three-body energy $\sqrt{s}$ and scales with an irrelevant normalization N. Here, q_1, and q_2 are outgoing π^- momenta that must be symmetrized later, q_3 is the outgoing π^+ momentum, and $E_x = \sqrt{\boldsymbol{x}^2 + m_\pi^2}$ here and in the following. The term $(m_\tau^2 - s)^2$ accounts for the $\tau \to W^- \nu_\tau$ decay vertex and the two-body phase space of the a_1 and the ν_τ of this process after integration over the neutrino angles [60]. See Fig. 1 for a graphical repre-
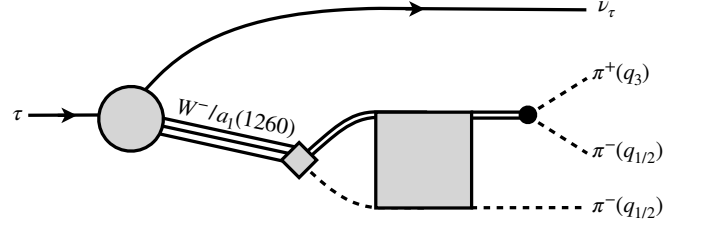

FIG. 1. Factorization of the (weak) production mechanism and (hadronic) final state three-body interaction. Full-directed, dashed, and double-full lines denote leptons, mesons and auxiliary ρ fields, respectively. The initial production mechanism is shown by a shaded circle and diamond corresponding to Eq. (9). The three-body unitary dynamics of the final pion states is depicted by the shaded rectangle, see Eq. (4)

sentation of the complete τ decay process. Furthermore, we chose $P_3 = (\sqrt{s}, \boldsymbol{0})$.

The amplitude $\hat{\Gamma}_{\Lambda\lambda} \equiv \hat{\Gamma}_{\Lambda\lambda}(\boldsymbol{q}_1, \boldsymbol{q}_2, \boldsymbol{q}_3)$ describes the decay of the axial $a_1(1260)$ resonance at rest with helicity Λ measured along the z-axis into a π^- and a $\rho_\lambda^0 \to \pi^+\pi^-$ with helicity λ,

$$
\hat{\Gamma}_{\Lambda\lambda}(\boldsymbol{q}_1, \boldsymbol{q}_2, \boldsymbol{q}_3) = \frac{1}{\sqrt{2}} \big[\Gamma_{\Lambda\lambda}(\boldsymbol{q}_1, \boldsymbol{q}_2, \boldsymbol{q}_3) - (\boldsymbol{q}_1 \leftrightarrow \boldsymbol{q}_2) \big], \tag{2}
$$

where

$$
\Gamma_{\Lambda\lambda}(\boldsymbol{q}_1, \boldsymbol{q}_2, \boldsymbol{q}_3) = \sqrt{\frac{3}{4\pi}} \mathfrak{D}_{\Lambda\lambda}^{1*}(\phi_1, \theta_1, 0) \times \tag{3}
$$
$$
v_\lambda^\pm(q_2, q_3) U_{\lambda L} \breve{\Gamma}_L(q_1),
$$

and

$$
\breve{\Gamma}_L(q_1) = \tau(\sigma(q_1)) \bigg[D_L(q_1) + \tag{4}
$$
$$
\int\limits_0^\Lambda \frac{\mathrm{d}p\, p^2}{(2\pi)^3} \frac{1}{2E_p} T_{LL'}^J(q_1, p) \tau(\sigma(p)) D_{L'}(p) \bigg].
$$

For readability (confusion with four-vector notation is excluded by context), we have abbreviated $D(x) := D(|\boldsymbol{x}|)$, $\breve{\Gamma}(x) = \breve{\Gamma}(|\boldsymbol{x}|)$, $T(q_1, p) := T(|\boldsymbol{q}_1|, |\boldsymbol{p}|)$, and $\sigma(x) := \sigma(|\boldsymbol{x}|)$ where the two-body invariant mass squared is denoted by

$$
\sigma(x) = s + m_\pi^2 - 2\sqrt{s} E_x \,. \tag{5}
$$

The angular structure of the final $\pi\rho$ state is conveyed by the usual capital Wigner-D function, $\mathfrak{D}_{\Lambda\lambda}^J(\phi_1, \theta_1, 0)$ with angles θ_1 and ϕ_1 giving the polar and azimuthal angles of $\boldsymbol{q}_1$. Note that the third argument is set to zero in the current convention which is consistent with the ρ polarization vectors of Appendix A obtained through a boost and two rotations (no initial rotation about the z-axis).

Equation (3) contains the transformation from the JLS basis, with L denoting the orbital angular momentum between π and ρ and $J = S = 1$ for total and ρ spin, respectively, to the helicity basis; this transformation involves the matrix

$$U_{L\lambda} = \sqrt{\frac{2L+1}{2J+1}}(L01\lambda|J\lambda)(1\lambda00|1\lambda)$$
$$= \begin{pmatrix} \frac{1}{\sqrt{3}} & \frac{1}{\sqrt{3}} & \frac{1}{\sqrt{3}} \\ \frac{1}{\sqrt{6}} & -\sqrt{\frac{2}{3}} & \frac{1}{\sqrt{6}} \end{pmatrix}, \qquad (6)$$

expressed by Clebsch-Gordan coefficients [79], and $U_{\lambda L} = U_{L\lambda}^T$, while we sum over identical indices L and L' in Eqs. (3) and (4), respectively.

The final decay vertex $v^\pm$ for $\rho^0 \to \pi^+\pi^-$ in Eq. (3) reads

$$v_\lambda^\pm(q_2, q_3) = I' v_\lambda(q_2, q_3), \qquad (7)$$
$$v_\lambda(q_2, q_3) = -ig_1 \epsilon_\lambda^\mu(\boldsymbol{q}_1)\,(q_2 - q_3)_\mu, \qquad (8)$$

where q_2, q_3 denote four-momenta, g_1 is the $\rho\pi\pi$ coupling, v_λ is the isospin-1 projected decay vertex, and I' describes the transition from isospin to particle basis as needed only in the final ρ decay. Note that the latter factor is irrelevant as long as there is only one isobar (ρ^0). Then, this factor can be reabsorbed into the overall normalization of the a_1 decay.

Continuing with the description of Eq. (4), the ρ propagator τ is discussed in more detail in Sec. II A. Furthermore, the $a_1 \to \rho\pi$ vertex, D, in Eq. (4) is directly parametrized in the JLS basis as

$$D_{L'}(p) = \left(D_{fL'} + \frac{m_\pi^2 \sqrt{c_{L'L'}^{(-1)}}D_{\tilde{f}}}{s - m_{a_1}^2} \right) \left(\frac{p}{m_\pi} \right)^{L'}, \quad (9)$$

where $D_{fL'}$ for $L' = 0, 2$ and $D_{\tilde{f}}$ are free parameters that are fit to the lineshape accounting, as well, for its unknown overall normalization. The quantity m_{a_1} is the expansion point of the three-body force and $c_{L'L'}^{(-1)} > 0$ is an expansion parameter (see below). Its square root may be understood as a bare $a_1\pi\rho$ coupling.

The quantity $T_{LL'}^J$ in Eq. (4) is the isobar-spectator amplitude in the JLS basis given by

$$T_{LL'}^J(q_1, p) = \left(B_{LL'}^J(q_1, p) + C_{LL'}(q_1, p) \right) + \qquad (10)$$
$$\int_0^\Lambda \frac{\mathrm{d}l\, l^2}{(2\pi)^3 2E_l} \left(B_{LL''}^J(q_1, l) + C_{LL''}(q_1, l) \right) \tau(\sigma(l)) T_{L''L'}^J(l, p),$$

where summation over L'' is implied. Note that the indices correspond to matrix notation, i.e., the first indices L and q_1 label outgoing (angular) momentum while the second indices p and L' label incoming (angular) momentum (similarly, in Eqs. (3) and (4)). The integrations in Eq. (4) and (10) have been regularized by the same cutoff Λ in contrast to Ref. [46] where covariant form factors

were used. We prefer here a hard cutoff because it simplifies the analytic continuation as discussed in Sec. III which also contains the in-depth description of the contours for the integrations in Eqs. (4) and (10).

In Eq. (10) the $\pi\rho$ interaction term B is complex-valued as demanded by three-body unitarity [41] and obtained from the plane-wave expression in isospin $I = 1$,

$$B_{\lambda\lambda'}(\boldsymbol{p}, \boldsymbol{p}') = \frac{v_\lambda^*(P - p - p', p)v_{\lambda'}(P - p - p', p')}{2E_{p'+p}(\sqrt{s} - E_p - E_{p'} - E_{p'+p} + i\epsilon)}, \qquad (11)$$

by projecting it to angular momenta $L^{(\prime)} \in \{S, D\}$ via

$$B_{\lambda\lambda'}^J(q_1, p) = 2\pi \int_{-1}^{+1} dx\, d_{\lambda\lambda'}^J(x) B_{\lambda\lambda'}(\boldsymbol{q}_1, \boldsymbol{p}), \qquad (12)$$

where $d_{\lambda\lambda'}^J(x = \cos\theta)$ denotes the small Wigner-d function and θ is the $\pi\rho$ scattering angle. Subsequently, the JLS expression is obtained by a linear transformation,

$$B_{LL'}^J(q_1, p) = U_{L\lambda} B_{\lambda\lambda'}^J(q_1, p) U_{\lambda'L'}, \qquad (13)$$

with $U_{L\lambda}$ from Eq. (6) and, as before, λ', L', p (λ, L, q_1) label the incoming (outgoing) state.

Three-body unitarity allows for additional terms of the $\pi\rho$ interaction that need to be real in the physical region [41]. We refer to such terms as contact terms or three-body forces that are generically parametrized by a Laurent series in the JLS basis ($L^{(\prime)} \in \{S,D\}$),

$$C_{LL'}(p, p') = \sum_{i=-1}^{\infty} c_{LL'}^{(i)} \left(\frac{s - m_{a_1}^2}{m_\pi^2} \right)^i \frac{p^L p'^{L'}}{m_\pi^{L+L'}}, \qquad (14)$$

including first-order poles to account for explicit resonances.

We fit the parameters m_{a_1}, $c_{00}^{(-1)}$, and $c_{00}^{(0)}$ with all other parameters set to zero, meaning that the C-term couples directly to the $S \to S$-wave transition but only indirectly to D-wave through the B-term (13). The analysis shows that this restriction is sufficient to fit the lineshape data as discussed in Sec. IV. Of course, in future fits to actual Dalitz plots the data become more sensitive to the partial-wave content and we expect that more fit parameters and channels are needed.

To fit the a_1 lineshape one needs to continue $\check{\Gamma}$ to real spectator momenta and perform the phase space integration over the final three-pion state. This is described in detail in Ref. [46] but not repeated here because it is of no relevance for the analytic continuation to the resonance pole discussed below.
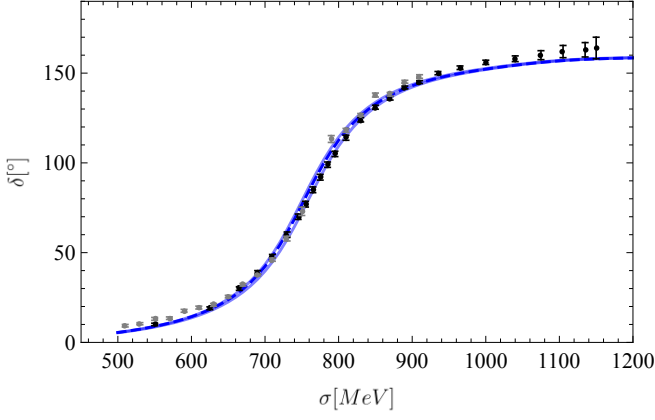
FIG. 2. The phaseshift from Eq. (20) with free parameters a_0 and a_1 fitted to data from Refs. [80] (black circles) and [81] (gray circles). We show here only the phase shifts corresponding to the three best fits quoted in Table I.

A. Two-body input

The ρ propagator τ of Eq. (4) reads, in a twice subtracted representation,

$$\tau^{-1}(\sigma) = K^{-1}(\sigma) - \Sigma(\sigma),$$

$$\Sigma(\sigma) = \int\limits_0^\infty \frac{\mathrm{d}k\, k^2}{(2\pi)^3} \frac{1}{2E_k} \frac{\sigma^2}{\sigma'^2} \frac{\tilde{v}(k)^*\tilde{v}(k)}{\sigma - 4E_k^2 + i\epsilon},$$

$$\sigma' = (2E_k)^2, \quad \tilde{v}(k) = \sqrt{\frac{16\pi}{3}}\, g_1 k \tag{15}$$

with a convergent selfenergy Σ and a regular K-matrix like quantity. In that, the former is expressed in terms of the vertex $\tilde{v}$ projected to the the $I = 1$ P-wave (spin $S = 1$) quantum numbers. This vertex can be obtained by considering the first-order Born series for the $\pi(k_1)\pi(k_2) \to \pi(k_1')\pi(k_2')$ scattering amplitude in the two-body rest frame, i.e., $k_1^{(\prime)} + k_2^{(\prime)} = (\sqrt{\sigma}, \mathbf{0})$, $k_1^{(\prime)\mu} - k_2^{(\prime)\mu} = (0, 2\mathbf{k}^{(\prime)})$. Using the $\rho\pi\pi$ vertex from Eq. (8) this reads

$$T_\rho(\sigma, z) = nI_\rho \frac{\sum_\lambda v_\lambda(k_1, k_2)v_\lambda^*(k_1', k_2')}{\sigma - m_\rho^2} = \frac{g_1^2}{\sigma - m_\rho^2}\, 4kk'z, \tag{16}$$

where $z = (\mathbf{k}, \mathbf{k}')/kk'$, $I_\rho = 2$ is a factor for isospin-1, and $n = 1/2$ is a symmetry factor. The second equal sign in Eq. (16) is due to the general properties of the helicity state vectors, c.f. Eq. (A3). Projecting this amplitude to

the P-wave amounts then to

$$T_\rho^1(\sigma) = 2\pi \int\limits_{-1}^1 \mathrm{d}z\, P_1(z)\, T_\rho(\sigma, z) \tag{17}$$

$$= \left(\sqrt{\frac{16\pi}{3}}\, g_1 k\right) \frac{1}{\sigma - m_\rho^2} \left(\sqrt{\frac{16\pi}{3}}\, g_1 k'\right)$$

$$=: \frac{\tilde{v}(k)\tilde{v}(k')}{\sigma - m_\rho^2},$$

defining the projected vertex $\tilde{v}$.

The two-body dynamics is encoded in $\tilde{v}$ but also in K of Eq. (15) that is very similar to a K-matrix up to the selfenergy Σ that contains also a real part. With K being a regular function in invariant-mass squared of the two-body system in the physical region, we found that two subtractions are sufficient to capture the relevant dynamics, i.e.,

$$K^{-1}(\sigma) = a_0 m_\pi^2 + a_1\sigma. \tag{18}$$

Here, the parameters a_i are fitted to the $\pi\pi$ phaseshift data by introducing the two-to-two on-shell T-matrix for $I = S = 1$,

$$T_{22}(\sigma) = \tilde{v}(k_{\rm cm})\tau(\sigma)\tilde{v}^*(k_{\rm cm}), \tag{19}$$

where $\tilde{v} = \tilde{v}^*$ and $k_{\rm cm} = \sqrt{\sigma/4 - m_\pi^2}$. The connection to the vector, isovector phaseshift δ^{11} is given by

$$\delta^{11}(\sigma) = \tan^{-1}\left(\frac{\mathrm{Im}\,T_{22}(\sigma)}{\mathrm{Re}\,T_{22}(\sigma)}\right), \tag{20}$$

which depends on g_1 from Eq. (8) and a_0, a_1 from Eq. (18) [1]. The parameters a_0 and a_1 are then fitted to experimental phaseshifts from Refs. [80, 81]. These parameters and the corresponding pole position of the ρ are given in the left column of Table I and the fit is shown in Fig. 2. As can be seen in the figure, the two sets of data are not in perfect agreement. In order to account for this source of systematic uncertainty we perform two additional fits. The first is only to data from Ref. [80], the second one is only to the data of Ref. [81]. These two fits are shown in the middle and right column of Tab. I. The systematic uncertainties that they introduce for the ρ pole position are far larger than statistical uncertainties calculated from a resampling of the combined data. From them, we calculate the ρ pole position with uncertainty to be $\sqrt{\sigma_\rho} = (754(3) - i\,72(1))$ MeV. The real part of this value is well below the PDG average of (775.26 ± 0.25) MeV, but is more in line with other fits to the same data, for instance in Refs. [82, 83]. Note that in Table I we only show the central values for parameters

----

[1] However, g_1 is fully correlated with a_0 and a_1 so that we fix it at $g_1 = 6$.

fitted data	[80] and [81]	[80]	[81]
a_0	-0.4604	-0.4712	-0.4639
$a_1 \cdot 10$	0.1556	0.1571	0.1567
Re $\sqrt{\sigma_\rho}$ [MeV]	754	758	753
Im $\sqrt{\sigma_\rho}$ [MeV]	-72	-71	-71

TABLE I. Fitted parameters of the two-body subsystem according to Eq. (18), and $\rho(770)$ meson pole positions $\sqrt{\sigma_\rho}$. Only central values are shown but uncertainties and correlations are fully propagated to the three-body calculation for the combined-data fit.

and pole position, but for the fit to the combined phase-shift data, uncertainties will be properly propagated to the three-body sector through resampling as described in Sec. IV B.

Note that it is possible to introduce more than two subtractions. Naturally, this leads to a better fit quality and can even be used to regularize the three-body equation: Indeed, more subtractions lead to higher powers of σ in the numerator of Σ of Eq. (15) which translate to higher powers of spectator momentum l in the denominator of τ due to Eq. (5), that is: $\lim_{l\to\infty} \sigma(l) \sim l$. Every additional subtraction contributes with $1/l$ to the convergence of Eq. (10), and with n subtractions one obtains $\lim_{l\to\infty} \tau(\sigma(l)) \sim l^{1-n}$. The crucial disadvantage of this method is the occurrence of of higher-order subtraction polynomials in the denominator of τ which can lead to unphysical poles on the first Riemann sheet; such artifacts must be avoided, especially if one aims at extracting pole positions in the complex plane. Therefore, we continue with two subtractions as described before.

In summary, we have employed the same, polarization vector-based spin-1 formalism for the two-body input as for the isobar-spectator interaction B in Eq. (11). This ensures three-body unitarity through the covariant parametrization of the ρ decay [41]. Additionally, the subtraction formalism for the loop term allows one to naturally regularize it and introduce the necessary freedom to parametrize the two-body input; after all, the formalism provides an efficient parametrization of the on-shell two-body input which is all that is needed in the three-body calculation (possibly below the $\pi\pi$ threshold, depending on the spectator momentum cutoff Λ).

III. ANALYTIC CONTINUATION

The key ingredient of the discussed a_1-production mechanism is the integral equation (10) solved for the $\pi\rho$ scattering amplitude. This equation is solved by replacing the integrations over the real-valued magnitude of the meson momenta by complex values along certain contours described in the following. Additionally, and in view of the final goal of this study – determination of the $a_1(1260)$ resonance pole – one needs to analytically continue the scattering amplitude (10) in the three-body
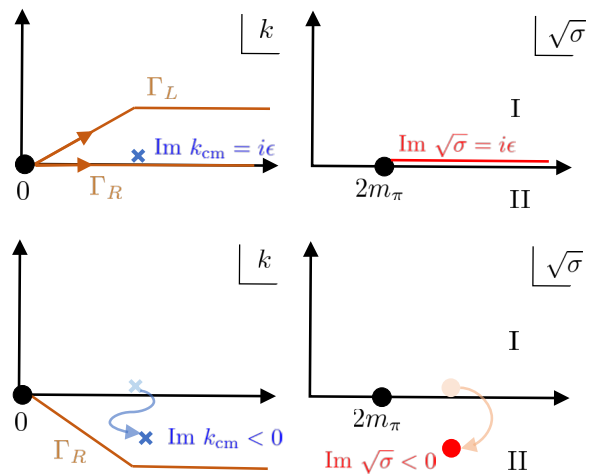

FIG. 3. Contours in two-body scattering. Upper row: Momentum integration (left) and physical amplitude (right) at $\sqrt{\sigma}+i\epsilon$ on the first ("I") Riemann sheet. Lower row: Momentum integration and amplitude on unphysical sheet II with Im $\sqrt{\sigma} < 0$. See text for additional explanations.

energy $\sqrt{s}$ to complex values.

Specifically, two types of integrations occur: (1) in $l := |\boldsymbol{l}|$ within the integral equation (10); and (2) in $k := |\boldsymbol{k}|$ within the selfenergy term of the two-body subsystem (15). The corresponding complex contours can be chosen individually and are referred to in the following as 'spectator momentum contour' (SMC) and 'selfenergy contour' (SEC), respectively. Both contours start at the respective origins, $l = k = 0$, and end at $l = \Lambda$ and $k = \infty$, respectively. In between these limits, different choices for the contours define different Riemann sheet in $\sqrt{s}$ as discussed in the following.

A similar discussion of the analytic structure in the context of dynamical coupled-channel approaches can be found in Ref. [84] for the Jülich/Bonn/Washington approach [85–87] and in Ref. [88] for the EBAC/ANL-Osaka approach [89, 90]. There is also a discussion in Ref. [60] on analytic continuation, but the structure of the scattering equation is substantially different because it does not contain three-body cuts from pion exchange as demanded by three-body unitarity [41]. In Ref. [84], a continuation obtained by certain approximations for three-body cuts was discussed, but the method proposed here is rigorous. For the sake of better readability and understanding, the following discussion is quite explicit and includes the simple two-body case, as well.

Regarding the cutoff used in this work, regularization is often achieved with form factors, and the SMC is given by a straight line from $l = 0$ into the lower complex-momentum half-plane; see, e.g., Refs. [46, 85, 91, 92]. We refrain from the use of form factors because they make the analytic structure of the amplitude unnecessarily complicated.
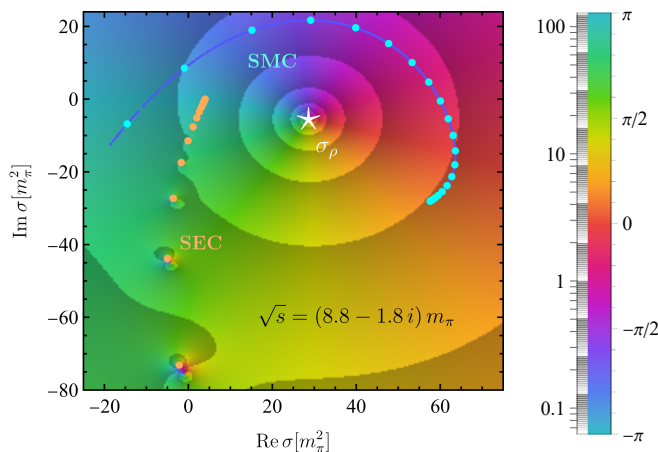
FIG. 4. Example for SMC and SEC contours in the complex plane of the two-body energy-squared, σ. Typical Gauss node distributions on the contours are indicated with turquoise and orange dots, respectively. The shading and coloring indicate magnitude and phase ϕ of $\tau = |\tau|e^{i\phi}$, respectively. The ρ pole at $\sigma = \sigma_\rho$ is highlighted with the white star. See text for further explanations.

A. Two-body scattering

To discuss the analytic structure, we recall that the placement of cuts is a choice. Cuts are the curves along which different Riemann sheets are analytically "glued" together. For example, a common choice in two-body scattering is to run the physical, right-hand cut along the real axis from threshold to ∞ in the two-body energy-squared σ. This simplifies the formulation of the dispersion relations and provides a convenient definition of the first and second Riemann sheet. With that definition, resonance poles can only to be found on the second, "unphysical" Riemann sheet as demanded by causality (see, e.g., Ref. [93] for a proof).

In contrast to cuts, the position of a branch point is fixed in s and σ for three- and two-particle scattering, respectively. Branch points define thresholds and arise whenever the pertinent momentum integrations begin in singularities or branch points themselves [84]. This is illustrated in Fig. 3 for the two-body case above threshold. The placement of the SEC producing the physical amplitude is constrained by the $+i\epsilon$ term in Eq. (15). In the figure, two possible integration contours are depicted, passing the singularity at $k = k_{\mathrm{cm}} + i\epsilon$ either on the right (Γ_R) or left (Γ_L). The former does not change the sign of (Im Σ) and, thus, yields the physical amplitude (19) describing experimental measurements at real energies. In contrast, choosing Γ_L leads to a sign change in (Im Σ) and an unphysical T_{22} on sheet II (still, at the same $\sigma = \sigma_{\mathrm{phys}} + i\epsilon$).

The physical and unphysical scattering amplitudes T_{22} are connected to each other, smoothly building the 2^N Riemann sheets (N being the number of two-body

thresholds). By convention, the physical amplitude on sheet I in the upper half-plane of $\sigma \in \mathbb{C}$ is connected along the real axis, $\sigma \in [4m_\pi^2, \infty)$, to the unphysical sheet II in the lower half-plane. For energies with Im $\sigma < 0$ (see Fig. 3, lower right), the amplitude on sheet II can be obtained by deforming the SEC as shown to the lower left. In particular, the two-body singularity at $k_{\mathrm{cm}} = \sqrt{\sigma/4 - m_\pi^2}$ also acquires a negative imaginary part, but a smooth deformation of Γ_R ensures that the SEC still passes the two-body singularity to the right, thus guaranteeing that the amplitude has been analytically continued from physical scattering energies σ to the second sheet in the lower half-plane, where resonance poles can be found.

In summary, passing the two-body singularity to the left or to the right (Γ_L vs. Γ_R) defines the Riemann sheet, except for one point at $\sigma = 4m_\pi^2$. There, the two-body singularity coincides with the lower limit of the integration, $k = k_{\mathrm{cm}} = 0$. Consequently, at this point there is no distinction between sheets, i.e., one is at the branch point that defines the two-pion threshold. We stress the (otherwise trivial) fact that a singularity in an integration limit induces a branch point, because it helps identifying branch points for the more complicated three-body case discussed in Sec. III C; see also Ref. [84].

In regard of the present application to the $a_1(1260)$ channel, we chose the SEC for the $\pi\pi$ subsystem in the ρ channel as

$$\Gamma_{\mathrm{SEC}} = \left\{ k | k = t + \frac{ic_1}{2} \arctan(c_2 t), t \in [0, \infty) \right\}, \quad (21)$$

with shape parameters c_1 and c_2 chosen such that this contour lies in the lower right quadrant of the k plane and always avoids the two-body singularity except at threshold,

$$\Gamma_{\mathrm{SEC}} \cap \{k_{\mathrm{cm}}\} \backslash \{0\} = \varnothing. \quad (22)$$

To display the SEC and the $\rho(770)$ resonance pole in the same plot, Γ_{SEC} is mapped to the σ plane according to $\sigma = 4(m_\pi^2 + k^2)$. The result is labeled "SEC" with the orange circles in Fig. 4 indicating the Gauss nodes chosen for numerical integration. As the figure shows, the chosen Γ'_R is sufficiently deformed to not only allow for the calculation of the physical amplitude but also for the calculation of τ in a large portion of unphysical sheet II, bound by the mapped SEC. This portion includes the ρ pole (white star). In other words, the so-defined two-body amplitude has its actual cut along the mapped SEC. Furthermore, instead of a discontinuity in σ along that cut, the amplitude exhibits a series of poles which is a consequence of the discretization in a finite number of Gauss nodes. This is made visible in the figure through the shading (repeated transitions from transparent to dark gray indicating increasing values of $|\tau|$), in addition to the color coding that indicates the phase ϕ of $\tau = |\tau|e^{i\phi}$. Notably, the ρ pole exhibits one full cycle $-\pi \to \phi \to +\pi$ (blue $\to$ red $\to$ green), indicat-

ing that the ρ pole is indeed a first-order singularity as required for a resonance.

The idea of suitably constructing contours to access the Riemann sheet(s) of interest, where resonance poles are situated, can be generalized to three-body scattering as discussed in the following. In particular, contour deformation replaces other methods of analytic continuation in which explicit discontinuities have to be added to the amplitude.

B. Three-body cuts

Before turning to the construction of a suitable spectator momentum contour (SMC) to access the $a_1(1260)$ pole, one needs to discuss three-body cuts because they must be avoided by the SMC. This is known since a long time and has been discussed in the context of the a_1 resonance in Ref. [94] (we adapt and extend the discussion here). These cuts arise from the pion-exchange term of Eq. (11) that is a direct consequence of three-body unitarity [41]. We note that this term corresponds to the forward going part of pion exchange only. If one adds the backward-going part, one recovers the covariant denominator $u - m_\pi^2 + i\epsilon$ [41] but we refrain from using this term because it can induce unphysical unitarity-violating imaginary parts above threshold if the regularization is not chosen correctly. Note also related but different discussions on sub-threshold behavior of this denominator vs. triangle graph in Ref. [29] and the comparison of the Feynman denominator and time-ordered perturbation theory in Ref. [45] where it was shown that the breaking of covariance in the latter is rather small.

It should also be noted that there will be a much more complicated analytic structure in unphysical regions of the amplitude which s-channel unitarity alone cannot fix (in analogy to two-body amplitudes). However, these structures are far away from the region in which we search for the a_1-pole and one can safely neglect them, i.e., the expansion of the C-term in the Laurent series of Eq. (14) is precise enough.

The denominator of Eq. (11) vanishes for any $x = \cos\theta \in [-1, 1]$ according to the partial-wave decomposition of Eq. (12). For a fixed three-body energy $\sqrt{s}$ and incoming spectator momentum p the singularities are given by

$$
p'_\pm = \frac{px(p^2 - \alpha^2) \pm \alpha\sqrt{(\beta + p^2(x^2 - 1))^2 - 4m_\pi^2\beta}}{2\beta},
$$
$$
\alpha(p) = \sqrt{s} - E_p, \quad \beta(p, x) = \alpha^2(p) - p^2x^2. \quad (23)
$$

The domain of real solutions is indicated in Fig 5 and bound by $p'_\pm(p, x = \pm 1)$.

Not all solutions p' are real as Fig. 6 shows. Notably, there are kinematic regions (e.g., $p = 3.4m_\pi$) in which the singularities fully enclose the origin which renders a naive integration from 0 to ∞, or to any physically required cutoff Λ, impossible. As a side remark, the small-
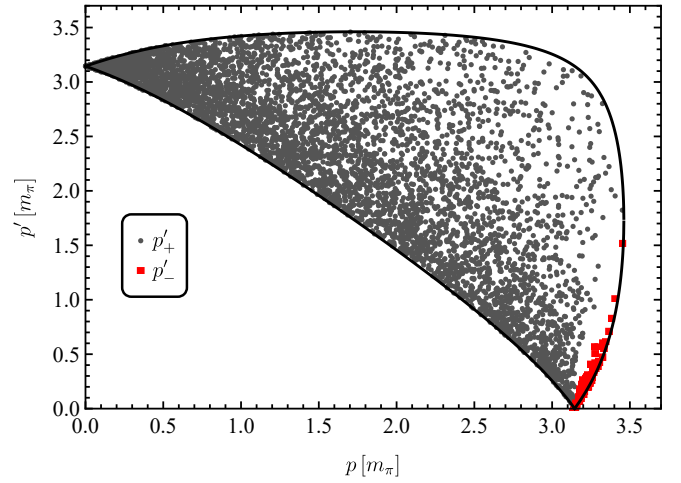

FIG. 5. Domain of real solutions $p'_\pm(p, x)$ according to Eq. (23) for $\sqrt{s} = 7.6\,m_\pi$. Gray and red dots represent individual solutions for some $x \in [-1, +1]$ which are enclosed by the $p'_\pm(p, x = \pm 1)$ boundary.
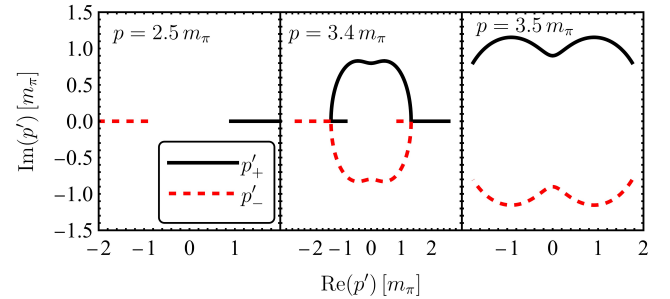

FIG. 6. Position of three-body singularities in $p'(p, x)$ for fixed p, $\sqrt{s} = 7.6\,m_\pi$, and $x \in [-1, 1]$ for solutions $p'_\pm$ according to Eq. (23).

est physically required cutoff $p_{\min}$ is given by the condition $\sigma(p) > 4m_\pi^2$ for the pions in the ρ selfenergy in Eq. (15) to be on-shell. Using Eq. (5), this leads to

$$
p_{\min}^2 = \frac{9m_\pi^4 - 10m_\pi^2 s + s^2}{4s}. \quad (24)
$$

Simultaneously, $p_{\min}$ must be large enough to cover all physically allowed momenta in the pion-exchange, given by the extension of the domain shown in Fig. 5 that can be determined through the vanishing argument of the square root of Eq. (23) at $x = 1$,

$$
\beta^2(p_{\min}, 1) - 4m_\pi^2\beta(p_{\min}, 1) = 0. \quad (25)
$$

The solution of this equation is also given by Eq. (24) as expected.

The crucial point is that the positions of the three-body singularities in p' depend on the value of p itself. For a suitably chosen contour SMC with $p \in \Gamma_{\mathrm{SMC}}$ and $p' \in \Gamma_{\mathrm{SMC}}$, the three-body cuts "open up" and allow for the integration of the scattering equation (10) as known

since a long time [95]. See also Ref. [96] for a similar numerical scheme in the context of Muskhelishvili-Omnés equations.
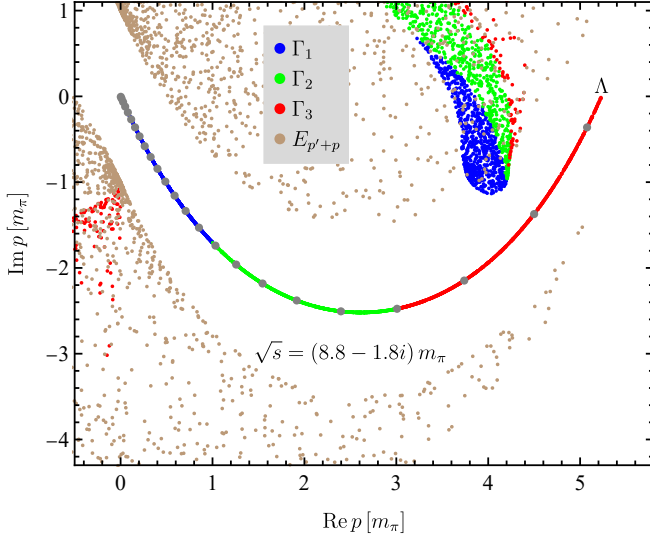

FIG. 7. Three-body singularities at fixed, complex 3-body energy $\sqrt{s}$. The color-coded dots show both solutions p' of Eq. (23) for different $p \in \Gamma_1$ (blue), $p \in \Gamma_2$ (green), $p \in \Gamma_3$ (red), and $x \in [-1, 1]$. Solutions $p'(p, x)$ for $E_{p+p'} = 0$ from Eq. (11), $p \in \Gamma_{\mathrm{SMC}}$, and $x \in [-1, 1]$ are indicated in light brown.

The precise form of the SMC is not fixed. We choose the smooth contour depicted in Fig. 7 that is split into different color-coded segments, $\Gamma_{\mathrm{SMC}} = \bigcup_{i=1}^{3} \Gamma_i$, to show which parts of the SMC correspond to which positions of three-body singularities, indicated with the dot clouds for both p_+ and p_-. Additionally, the singularities $p'(p, x)$ of the $1/E_{p'+p}$ term in Eq. (11) are indicated by brown dots irrespective of the value of $p \in \Gamma_{\mathrm{SMC}}$. The SMC is parametrized as

$$\Gamma_{\mathrm{SMC}} = \{p | p = t + iV_0(1 - e^{-t/w}) \\ \times (1 - e^{(t-\Lambda)/w}), \ t \in [0, \Lambda]\}. \quad (26)$$

This expression contains a parameter for the initial and final slope, w, and another one for the extension of the SMC into the lower half-plane, V_0. In general, a larger V_0 allows one to go further into the complex $\sqrt{s}$ plane to look for poles; piecewise-straight contours are also possible, in general, but require more integration nodes than smooth paths for a given precision. An example of integration nodes is shown in Fig. 7 with the gray circles on top of Γ_{SMC}.

To avoid singularities of the B-term one simply ensures that Γ_{SMC} never overlaps with the solutions of Eq. (23),

$$\Gamma_{\mathrm{SMC}} \cap \{p'(p \in \Gamma_{\mathrm{SMC}}, x \in [-1, 1])\} = \varnothing \, ; \quad (27)$$

similarly, for the $E_{p'+p}$ term,

$$\Gamma_{\mathrm{SMC}} \cap \{p' | E_{p'+p} = 0, p \in \Gamma_{\mathrm{SMC}}, x \in [-1, 1]\} = \varnothing \, . \quad (28)$$

There is a region of $\sqrt{s}$ in the lower complex half-plane for which this is the case, and the extent of that region depends on Γ_{SMC}. We have made sure that with the SMC of Eq. (26) the corresponding $\sqrt{s}$-region covers the pole region of the $a_1(1260)$ well.

C.   Real and complex threshold openings

In Sec. III A we have already discussed the analytic structure of the two-body amplitude, its (threshold) branch point at $\sigma = 4m_\pi^2$, where the two Riemann sheets coincide, and the ρ pole on the second Riemann sheet. We now discuss this amplitude in the presence of the SMC, i.e., the two-body system being a subsystem of the three-body amplitude with the spectator momentum being on the SMC.

Figure 4 shows the SEC mapped to the σ plane by $\sigma = 4E_k^2$. It also shows the SMC mapped to this plane via Eq. (5). This representation has the advantage that a crossing of SEC and SMC in the figure directly indicates a zero of the selfenergy denominator $(\sigma - 4E_k^2)$ of Eq. (15) that has to be avoided,

$$\sigma(p^2) \neq 4E_k^2 \ \forall \ p \in \Gamma_{\mathrm{SMC}} \wedge k \in \Gamma_{\mathrm{SEC}} \, . \quad (29)$$

The last condition is that neither contour can cross the ρ pole at σ_ρ, except for $p = 0$,

$$\sigma(p^2) \neq \sigma_\rho \ \forall p \in \Gamma_{\mathrm{SMC}} \backslash \{0\} \ \wedge \ 4E_k^2 \neq \sigma_\rho \ \forall k \in \Gamma_{\mathrm{SEC}} \, . \quad (30)$$

The conditions (22, 27-30) constitute the complete set of rules to access all Riemann sheets in the problem.

The exclusion of $p = 0$ in Eq. (30) can be understood in the context of branch points. According to Eq. (5), the condition $p = 0$ and $\sigma = \sigma_\rho$ corresponds to $\sqrt{s} = \pm\sqrt{\sigma_\rho} + m_\pi$. In other words, at these complex three-body energies, the spectator momentum integration starts at the ρ pole. According to Sec. III A, if an integration limit coincides with a singularity, a branch point is generated. Therefore, taking only the square root of interest (positive Re $\sqrt{\sigma_\rho}$) and invoking the Schwarz reflection principle, we conclude that the three-body amplitude has branch points at $\sqrt{s} = \sqrt{s_\rho} := \sqrt{\sigma_\rho} + m_\pi$ and $\sqrt{s} = \sqrt{s_\rho}^* = \sqrt{\sigma_\rho}^* + m_\pi$. We refer to them as $\pi\rho$ branch points in the following.

There is a third branch point: the two-body threshold induces the real-valued 3-body threshold at $s = (3m_\pi)^2$ because at that energy and $p = 0$, we have $\sigma = 4m_\pi^2$ according to Eq. (5). In other words, the spectator momentum integration starts at the two-body branch point, which induces another branch point in the three-body amplitude. In Ref. [97] additional properties of these branch points were discussed.

The overall analytic structure of the three-body amplitude of Eq. (10) is visualized in Fig. 8. It shows the real branch point at $\sqrt{s} = 3m_\pi$ with its associated cut chosen along the real $\sqrt{s}$ axis defining sheets I and II.
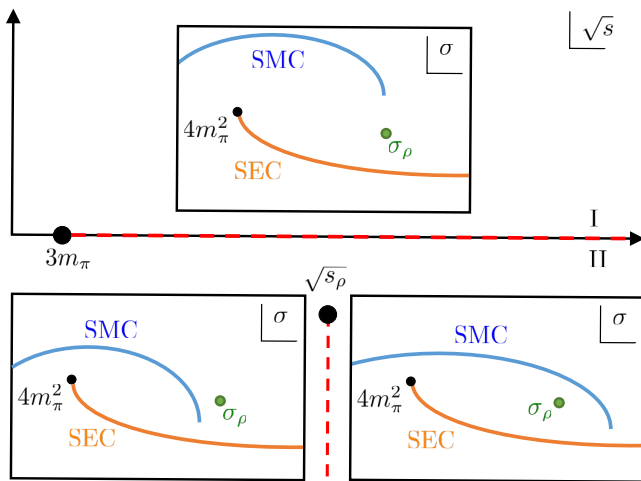
FIG. 8. Analytic structure of the 3-body amplitude in the $\sqrt{s}$ plane. The real and complex branch points (thick black dots) are shown together with their respective cuts (red dashed lines). The $\pi\rho$ branch points lie on sheet II and induce additional sheets III and IV (not shown). The insets show the SMC mapped to the σ plane (blue lines), in a qualitative way. Its position changes according to the approximate value of $\sqrt{s}$ where the insets are placed. In the σ plane, the SEC (orange lines) starting at the $\pi\pi$ threshold (small black dots) does not change if $\sqrt{s}$ changes, but the SMC does.

Also, the figure shows one of the complex branch points at $\sqrt{s} = \sqrt{s_\rho}$ which is situated on sheet II. The cut associated with the complex branch point is conveniently run into the negative imaginary $\sqrt{s}$-direction so that the shown Riemann sheet is the region closest to the physical axis. If regions behind that cut ought to be explored (defined as sheet III), more complicated contours must be chosen [84].

In addition, the insets in Fig. 8 show the σ plane with the SMC and SEC similar as in Fig. 4. The position of the insets in the $\sqrt{s}$ plane qualitatively corresponds to the $\sqrt{s}$ used to map the SMC to the σ plane, according to Eq. (5). Note how the position of the SMC changes relative to the ρ pole at σ_ρ. For example, for $\sqrt{s}$ to the left (right) of the $\pi\rho$ branch cut, the SMC passes the ρ pole to the left (right).

In Fig. 9 we show a typical picture of $|T_{00}|$ of Eq. (10) with the integration contours defined in Eqs. (21) and (26). The shape parameters that allow access to a sufficiently large region in the broad vicinity of the $a_1(1260)$ pole, and which make the cut of the $\pi\rho$ branch point run approximately in the negative-imaginary $\sqrt{s}$ direction, are given in Table II. The a_1 pole is always to the lower right of the $\pi\rho$ branch point in the $\sqrt{s}$ plane as Fig. 9 shows. Therefore, the qualitative positions of SEC and SMC in the σ plane, corresponding to $\sqrt{s}$ taking the value of the a_1 pole, are given by the lower right inset of Fig. 8 which is also the situation shown in Fig. 4. Similar to Fig. 4, the cut induced by $\sqrt{s_\rho}$ is approximated by a series of poles due to the numerical discretizations, as
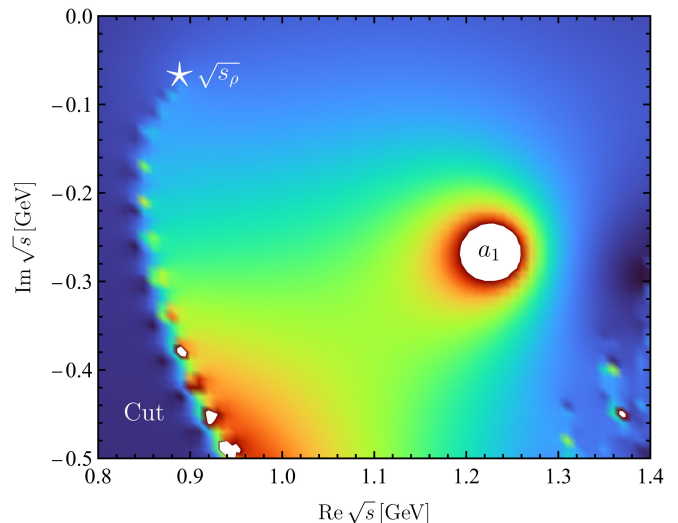

FIG. 9. Typical amplitude $|T_{00}|$ of Eq. (10), color coded from small values (dark blue) to large values (red; maxed-out values at white). The $a_1(1260)$ pole, $\pi\rho$ branch point at $\sqrt{s} = \sqrt{s_\rho}$ and its associated cut are also indicated. See text for further explanations.

$c_1\,[m_\pi]$	$c_2\,[m_\pi^{-1}]$	$w\,[m_\pi]$	$V_0\,[m_\pi]$
-7.16	0.418	1.433	-3.58

TABLE II. Shape parameters for the SEC in Eq. (21) and SMC in Eq. (26).

Fig. 9 shows. While in the former case this was due to the self-energy integration, in the latter case it is due to the integration over the spectator momentum.

While Fig. 9 and all results in this paper have been obtained using the shape parameters of Table II, the figure also shows that this choice is not universally valid for all three-body energies. In the lower right-hand corner (highest energies, farthest into the complex plane), we observe numerical fluctuations. These are poles induced by a three-body singularities coinciding with the SMC as illustrated in Fig. 7; they correspond to violations of Eqs. (27) or (28). If the analytic continuation in such regions of $\sqrt{s}$ is desired, one needs to choose a different SMC.

IV. RESULTS

A. Fit

The free parameters of the model are fixed by a fit to the lineshape for the decay $\tau^- \to \pi^-\pi^-\pi^+\nu_\tau$. Data for this process measured in the ALEPH experiment were originally published in Ref. [47]. In Ref. [98] the unfolding method was improved and an error was fixed (see the webite [99] for numerical values) . The data include cor-

relations that correspond to both systematic and statistical uncertainty. However, the systematic uncertainties are small relative to the statistical uncertainties, thus we neglect them. The χ^2 can then be calculated with the formula

$$\chi^2 = (\vec{D} - \vec{\mathcal{L}})^T \Sigma^{-1} (\vec{D} - \vec{\mathcal{L}}) , \qquad (31)$$

where Σ is the data covariance matrix, $\vec{D}$ is a vector containing the central values of the ALEPH line shape data and $\vec{\mathcal{L}}$ is a vector containing our prediction of the lineshape calculated with Eq. (1) as a function of $\sqrt{s}$ at each of the central values of energy for the ALEPH data. We fit the 65 data points in the range 0.55 GeV $< \sqrt{s} < 1.50$ GeV but do not include all correlations in Σ; instead we set all correlations to 0 except those between nearest neighbors. This choice is justified in Appendix B.

We fit the parameters c_{00}^{-1} and c_{00}^{0} from the expansion of the three-body term in Eq. (14). We do not include c_{00}^{1} or any higher c_{00} terms and we do include any c_{10}, c_{01}, or c_{11} terms because including these terms in the fit when $\Lambda = 0.73$ GeV increases the χ_{dof}^2. Fits for other values of Λ just serve to assess systematic effects and we do not try to change their parametrization. Thus, our fit of the lineshape has a total of 6 free parameters: c_{00}^{-1}, c_{00}^{0}, and m_{a_1} from Eq. (14), and D_{f0}, D_{f2}, and $D_{\tilde{f}}$ from Eq. (9).

The line shape depends on Λ in Eqs. (4) and (10). A cutoff of $\Lambda = 0.73$ GeV is the lowest possible value allowed by Eq. (24) if an upper limit of $\sqrt{s} = 1.5$ GeV is chosen for the fit. We consider the case $\Lambda = 0.73$ GeV to be our primary fit because it leads to the best χ^2 as shown in Table III. However, to study systematic effects, we also vary Λ, leaving the two-body input encoded in the parameters a_0 and a_1 unchanged, and perform several fits. We list the pole position and free parameters of these fits in Tab. III. As we increase Λ, m_{a_1} and c_{00}^{-1} decrease, whereas $c_{00}^{0} m_{a_1}$ increases. The pole position, however, remains relatively unchanged, which reassures us, because the physical pole position should not depend on the cutoff.

B. Discussion

The $a_1(1260)$ lineshape data and best fits for different cutoffs are shown in Fig. 10 with the solid lines. Fit uncertainties are indicated with the blue band for our main result ($\Lambda = 0.73$ GeV). For better visibility, the band width is multiplied by a factor of 10. The plot of reduced residuals for the $\Lambda = 0.73$ GeV case (bottom of Fig. 10) shows that there are no obvious systematic deviations of the fit from data, except maybe for a structure at $\sqrt{s} \approx 0.8$ GeV. Also, around that energy the fits for different Λ differ from each other more than in other energy regions, and a substantial fraction of the χ^2 for larger cutoffs Λ (see Table III) arises in this energy region. In general, however, the pertinent fits are all very
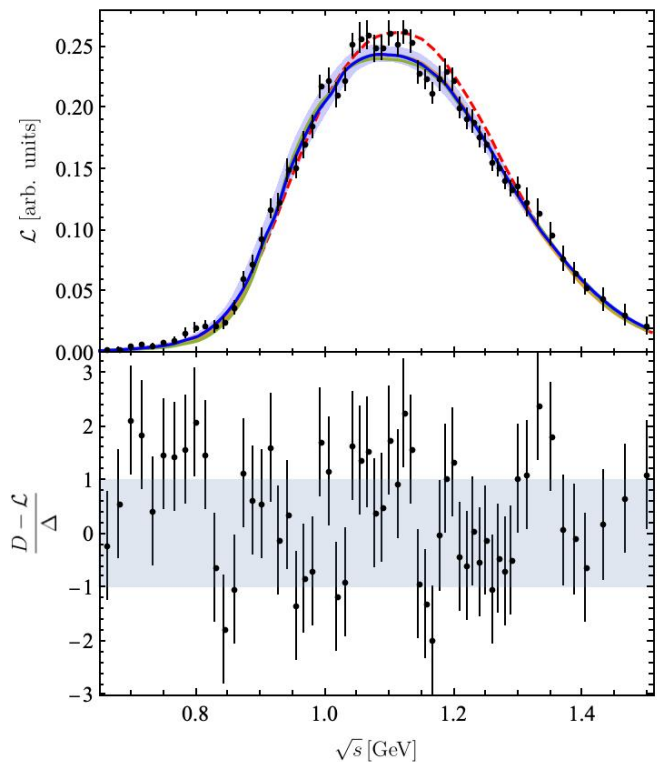

FIG. 10. The fit to the line shape data from the ALEPH experiment [98] (top) and the normalized residuals for the $\Lambda = 0.73$ GeV case (bottom), where $D - \mathcal{L}$ is a given residual and Δ the pertinent data uncertainty. In the upper figure, the blue band indicates the spread of the resampled fit with cutoff $\Lambda = 0.73$ GeV, multiplied by a factor of 10 for better visibility. The pertinent best fit is indicated with the blue solid line. Other best fits are also shown, for $\Lambda = 0.9$ GeV (orange), $\Lambda = 1.05$ GeV (green), and $\Lambda = 1.2$ GeV (red). In many of theses cases, the curves almost coincide. The red dashed line shows the calculation of the line shape with the same parameters as the $\Lambda = 0.73$ case with all D-wave terms set to 0. The difference between this curve and the blue one shows the contribution of the D-wave.

close together which is also reflected in the very small variation in pole positions indicated in Table III.

We show with a red dashed line in Fig. 10 the line shape with $\Lambda = 0.73$ GeV calculated with the D-wave contributions set to 0. The difference in this case from the blue line shows the contributions of the D-wave term. This difference is small, which is qualitatively in line with the PDG [1]. Note that this is a prediction at this point; the D-wave can only be determined more quantitatively once Dalitz plots are analyzed, as measured, e.g., by CLEO [9].

We test the impact of the rescattering term by performing a fit in which we exclude $B_{LL'}^J(q_1, p)$ from Eq. (10). This pion-exchange term is required by three-body unitarity [41] and omitted in Ref. [60]. As Table III (last row) and Fig. 11 (open red circle) show, the $a_1(1260)$ pole position is significantly shifted in the refit without the B-term. Still, Fig. 11 also shows that, even with-

Λ [GeV]	+0.73	+0.90	+1.05	+1.2	+0.73(no B)	+0.73 ([80] data)	+0.73 ([81] data)
Re $\sqrt{s_0}$ [GeV]	+1.232	+1.223	+1.231	+1.240	+1.174	+1.233	+1.230
Im $\sqrt{s_0}$ [GeV]	−0.266	−0.269	−0.244	−0.251	−0.252	−0.278	−0.261
$\chi^2/(65-6)$	0.99	1.32	1.60	1.90	2.56	0.99	0.98
c_{00}^{-1}	+16.48	+14.59	+12.67	+11.53	+20.16	+16.74	+16.49
c_{00}^{0}	+1.729	+1.750	+1.843	+2.073	+0.0191	+1.712	+1.720
m_{a_1} [GeV]	+1.293	+1.287	+1.281	+1.278	+1.391	+1.296	+1.294
$D_{f0} \times 10^7$ [a.u.]	−1.841	−2.371	−2.126	−2.250	−0.9249	−1.887	−1.829
$D_{f2} \times 10^8$ [a.u.]	+6.462	+3.094	+1.567	+0.837	−6.824	+6.718	+6.512
$D_{\tilde{f}} \times 10^6$ [a.u.]	−1.319	−1.358	−1.338	+1.372	−1.235	−1.329	−1.318

TABLE III. Best-fit pole positions $\sqrt{s_0}$ of the $a_1(1260)$, χ^2, and central values for fit parameters (uncertainties for pole positions are only quoted in the main text, for readability). There are 65 data points and six parameters. The column labeled "no B" shows our fits when we set the pion exchange term $B = 0$. The last two columns show variation from different two-body input as referenced in the label. The c-terms are unitless while the abbreviation "a.u." for the D-terms stands for "arbitrary units" because they contain the factor that connects to the un-normalized line shape data.
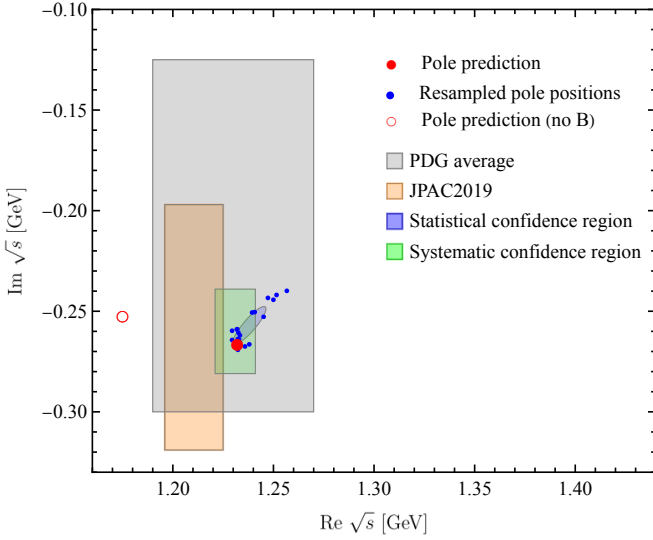

FIG. 11. Compilation of pole positions determined in this work including statistical and systematic uncertainties. For convenience, the PDG [1] average and a result by JPAC [60] are quoted as well. See text for further explanations.

using the different values of a_0 and a_1 calculated in the first step. From each of these fits, a pole position is calculated, shown with blue dots in Fig. 11. We also show the error ellipse keeping in mind that this is a non-linear fit problem.

The green rectangle in Fig. 11 shows the region of pole positions from different cutoffs Λ according to Table III. To that we add a second source of systematic uncertainties from the different two-body input according to the last two columns of Table III. Such variations in Λ help assess the influence of inherent model uncertainties so we add then as systematic error to our result for the $a_1(1260)$ pole position quoted in the next section. Our entire confidence region, including both statistical and systematic uncertainties, lies entirely within the PDG estimate of the $a_1(1260)$ denoted with the gray rectangle, and it is not in strong tension with the JPAC result [60] (orange rectangle).

We extract the residues of the pole position using the coupled-channel partial-wave amplitude of Eq. (10). It can be expanded in $\sqrt{s}$ around the pole position $\sqrt{s_0}$ of the $a_1(1260)$,

$$T_{LL'}^{J}(p,p') = \frac{\tilde{g}_L(p)\,\tilde{g}_{L'}(p')}{\sqrt{s}-\sqrt{s_0}} + \mathcal{O}(1), \qquad (32)$$

with $\tilde{g}_L$ playing the role of (Breit-Wigner) branching ratios, but defined at the pole [1]. In addition, for the current case of $\pi\rho$ scattering in S and D-waves, the $\tilde{g}$ are necessarily functions of spectator momentum, $\tilde{g}_L \equiv \tilde{g}_L(p)$. Analogously one might think of resonance transition form factors that are closely related to pole residues depending on photon virtuality [87, 100]. For a numerically stable method to calculate residues see Appendix C of Ref. [101]. We show the $\tilde{g}_L(p)$ for real spectator momenta p in Fig. 12, which requires another analytic extrapolation from the complex p on the spectator momentum contour (SMC) at which the solution is calculated.

As Fig. 12 shows, the a_1 resonance does couple to the $\pi\rho$ D-wave channel even if the corresponding coupling

out the B-term, our model is not identical to the one of JPAC [60] which might be due to other reasons like a slightly different treatment of the two-body input, different cutoffs, or the fact that in Ref. [60] the lineshape data of Ref. [47] is fitted, while we fit the data of Ref. [98].

We show our pole predictions in Fig. 11. Statistical uncertainties are calculated through a re-sampling procedure (blue dots). We calculate statistical uncertainty of the pole position using a resampling procedure. This is done in two steps. Firstly, the two-body data from Refs. [80] and [81] are resampled 20 times with a normal distribution using the given data uncertainties. Parameters a_0 and a_1 (given in Eq. (18)) are fit to each resampled set. Secondly, 20 sets of resampled ALEPH data [98, 99] are generated. A fit is performed for each resampled set
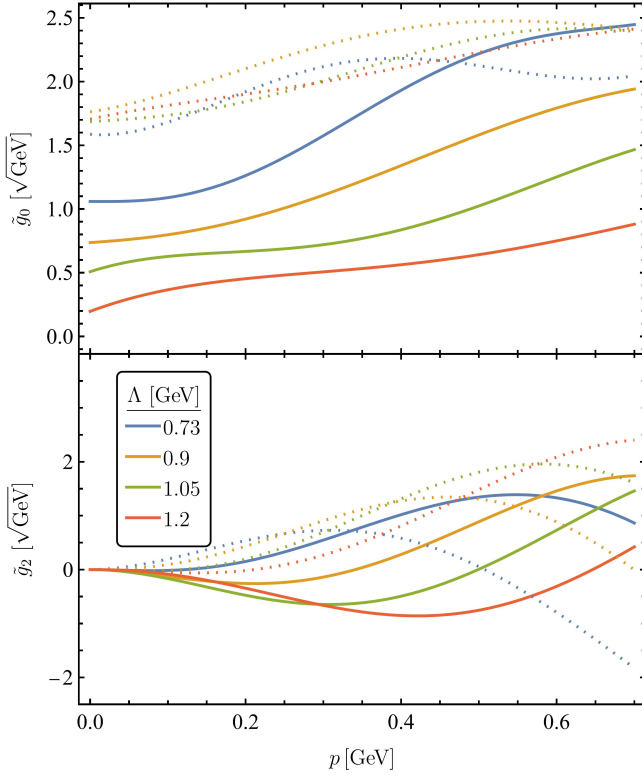
FIG. 12. Pole couplings according to Eq. (32) as a function of real spectator momentum p. These quantities play the role of spectator-momentum dependent branching ratios. Results for S-wave are shown at the top and for D-wave at the bottom, for different cutoffs Λ as indicated. The solid (dashed) lines show the real (imaginary) parts.

term appearing in Eq. (9) is not fitted, $c_{22}^{-1} = 0$, and, similarly, $c_{20}^{-1} = c_{02}^{-1} = 0$ in Eq. (14). This is due to the B-term which always allows for non-diagonal transitions between S and D-wave channels. Yet, the D-wave decay is clearly smaller than the S-wave decay, and the contribution to the lineshape from D-wave (at real energies) is very small, see Fig. 10. While our complex pole couplings are a prediction at this point, in future work they can be tested and even extracted from data by analyzing Dalitz plots of the a_1 decay such as measured at CLEO [9].

V. CONCLUSIONS

In this work we have detailed how the pole position of the $a_1(1260)$ meson can be determined using a manifestly unitary three-body formalism. The three-body dynamics of the decay is fully taken into account, including the line shape corrections due to the pion exchange (sometimes referred to as "rearrangement" graph). This process is a direct consequence of unitarity. It ensures that, apart from the usual isobar-spectator propagation in the s-channel, this is the only possible onshell arrangement of three pions. Also, the amplitude necessarily exhibits two independent integrations that cannot be simply recast and factorized into the phase space calculation, but that explicitly need to be performed.

Three-body cuts and the two integrations imply problems for the analytic continuation of the amplitude to the complex pole position of the $a_1(1260)$. We explain in detail how the continuation is achieved by contour deformation and how different Riemann sheets are induced by an appropriate choice of integration contours.

Upon implementation, we find that the pion exchange term does have significant influence on the pole position of the $a_1(1260)$; taking into account nearest-neighbor correlations in the data from ALEPH [98], the pole position is determined to be

$$\sqrt{s_0} = (1232^{+15+9}_{-0.2-11} - i(266^{+0.3+15}_{-22-27})) \text{ MeV}, \qquad (33)$$

where the first errors are statistical (including nearest-neighbor correlations) and the second ones are systematic, reflecting the cut-off dependence and two-body input according to Table III.

The current calculation is restricted to $\rho\pi$ channels in S and D-wave. In future upgrades to more coupled channels, like sub-dominant $\sigma\pi$, it will be possible to simultaneously fit line shape and Dalitz plots to exploit unitarity which relates these data.

[1] P. A. Zyla *et al.* (Particle Data Group), "Review of Particle Physics," PTEP **2020**, 083C01 (2020).

[2] H. Al Ghoul *et al.* (GlueX), "Measurement of the beam asymmetry Σ for π^0 and η photoproduction on the proton at $E_\gamma = 9$ GeV," Phys. Rev. **C95**, 042201 (2017), arXiv:1701.08123 [nucl-ex].

[3] M. Alekseev *et al.* (COMPASS), "Observation of a $J^{PC} = 1^{-+}$ exotic resonance in diffractive dissociation of 190-GeV/c π^- into $\pi^-\pi^-\pi^+$," Phys. Rev. Lett. **104**, 241803 (2010), arXiv:0910.5842 [hep-ex].

[4] D. M. Asner *et al.*, "Physics at BES-III," Int. J. Mod. Phys. **A24**, S1–794 (2009), arXiv:0809.1869 [hep-ex].

[5] C Adolph *et al.* (COMPASS), "Resonance Production and $\pi\pi$ S-wave in $\pi^- + p \to \pi^-\pi^-\pi^+ + p_{recoil}$ at 190 GeV/c," Phys. Rev. D **95**, 032004 (2017), arXiv:1509.00992 [hep-ex].

[6] M. Aghasyan *et al.* (COMPASS), "Light isovector resonances in $\pi^- p \to \pi^-\pi^-\pi^+ p$ at 190 GeV/c," Phys. Rev.

D **98**, 092003 (2018), arXiv:1802.05913 [hep-ex].

[7] M. Ablikim *et al.* (BESIII), "Study of the Decay $D_s^+ \to \pi^+\pi^+\pi^-\eta$ and Observation of the W-annihilation Decay $D_s^+ \to a_0(980)^+\rho^0$," (2021), arXiv:2106.13536 [hep-ex].

[8] M. Ablikim *et al.* (BES), "Resonances in $J/\psi \to \phi\pi^+\pi^-$ and ϕK^+K^-," Phys. Lett. B **607**, 243–253 (2005), arXiv:hep-ex/0411001.

[9] D. M. Asner *et al.* (CLEO), "Hadronic structure in the decay $\tau^- \to \nu_\tau\pi^-\pi^0\pi^0$ and the sign of the tau-neutrino helicity," Phys. Rev. D **61**, 012002 (2000), arXiv:hep-ex/9902022.

[10] M. Albrecht *et al.* (Crystal Barrel), "Coupled channel analysis of $\bar{p}p \to \pi^0\pi^0\eta$, $\pi^0\eta\eta$ and $K^+K^-\pi^0$ at 900 MeV/c and of $\pi\pi$-scattering data," Eur. Phys. J. C **80**, 453 (2020), arXiv:1909.07091 [hep-ex].

[11] R. Pasquier and J. Y. Pasquier, "Khuri-Treiman-Type Equations for Three-Body Decay and Production Processes," Phys. Rev. **170**, 1294–1309 (1968).

[12] I. J. R. Aitchison, "Relativistic Three Pion Dynamics Generated by Two-Body Unitarity and Analyticity," J. Phys. G **3**, 121 (1977).

[13] Gilberto Colangelo, Stefan Lanz, and Emilie Passemar, "A New Dispersive Analysis of $\eta \to 3\pi$," PoS **CD09**, 047 (2009), arXiv:0910.0765 [hep-ph].

[14] Bastian Kubis and Sebastian P. Schneider, "The Cusp effect in $\eta' \to \eta\pi\pi$ decays," Eur. Phys. J. C **62**, 511–523 (2009), arXiv:0904.1320 [hep-ph].

[15] Sebastian P. Schneider, Bastian Kubis, and Christoph Ditsche, "Rescattering effects in $\eta \to 3\pi$ decays," JHEP **02**, 028 (2011), arXiv:1010.3946 [hep-ph].

[16] Karol Kampf, Marc Knecht, Jiri Novotny, and Martin Zdrahal, "Analytical dispersive construction of $\eta \to 3\pi$ amplitude: first order in isospin breaking," Phys. Rev. D **84**, 114015 (2011), arXiv:1103.0982 [hep-ph].

[17] Franz Niecknig, Bastian Kubis, and Sebastian P. Schneider, "Dispersive analysis of $\omega \to 3\pi$ and $\phi \to 3\pi$ decays," Eur. Phys. J. C **72**, 2014 (2012), arXiv:1203.2501 [hep-ph].

[18] Peng Guo, Ryan Mitchell, Matthew Shepherd, and Adam P. Szczepaniak, "Amplitudes for the analysis of the decay $J/\psi \to K^+K^-\pi^0$," Phys. Rev. D **85**, 056003 (2012), arXiv:1112.3284 [hep-ph].

[19] I. V. Danilkin, C. Fernández-Ramírez, P. Guo, V. Mathieu, D. Schott, M. Shi, and A. P. Szczepaniak, "Dispersive analysis of $\omega/\phi \to 3\pi, \pi\gamma^*$," Phys. Rev. D **91**, 094029 (2015), arXiv:1409.7708 [hep-ph].

[20] Peng Guo, I. V. Danilkin, and Adam P. Szczepaniak, "Dispersive approaches for three-particle final state interaction," Eur. Phys. J. A **51**, 135 (2015), arXiv:1409.8652 [hep-ph].

[21] Peng Guo, Igor V. Danilkin, Diane Schott, C. Fernández-Ramírez, V. Mathieu, and Adam P. Szczepaniak, "Three-body final state interaction in $\eta \to 3\pi$," Phys. Rev. D **92**, 054016 (2015), arXiv:1505.01715 [hep-ph].

[22] J. T. Daub, C. Hanhart, and B. Kubis, "A model-independent analysis of final-state interactions in $\overline{B}_{d/s}^0 \to J/\psi\pi\pi$," JHEP **02**, 009 (2016), arXiv:1508.06841 [hep-ph].

[23] Franz Niecknig and Bastian Kubis, "Dispersion-theoretical analysis of the $D^+ \to K^- \pi^+ \pi^+$ Dalitz plot," JHEP **10**, 142 (2015), arXiv:1509.03188 [hep-ph].

[24] P. Guo, I. V. Danilkin, C. Fernández-Ramírez, V. Math-

ieu, and A. P. Szczepaniak, "Three-body final state interaction in $\eta \to 3\pi$ updated," Phys. Lett. B **771**, 497–502 (2017), arXiv:1608.01447 [hep-ph].

[25] Tobias Isken, Bastian Kubis, Sebastian P. Schneider, and Peter Stoffer, "Dispersion relations for $\eta' \to \eta\pi\pi$," Eur. Phys. J. C **77**, 489 (2017), arXiv:1705.04339 [hep-ph].

[26] M. Albaladejo and B. Moussallam, "Extended chiral Khuri-Treiman formalism for $\eta \to 3\pi$ and the role of the $a_0(980)$, $f_0(980)$ resonances," Eur. Phys. J. C **77**, 508 (2017), arXiv:1702.04931 [hep-ph].

[27] Franz Niecknig and Bastian Kubis, "Consistent Dalitz plot analysis of Cabibbo-favored $D^+ \to \bar{K}\pi\pi^+$ decays," Phys. Lett. B **780**, 471–478 (2018), arXiv:1708.00446 [hep-ph].

[28] Maximilian Dax, Tobias Isken, and Bastian Kubis, "Quark-mass dependence in $\omega \to 3\pi$ decays," Eur. Phys. J. C **78**, 859 (2018), arXiv:1808.08957 [hep-ph].

[29] A. Jackura, C. Fernández-Ramírez, V. Mathieu, M. Mikhasenko, J. Nys, A. Pilloni, K. Saldaña, N. Sherrill, and A.P. Szczepaniak (JPAC), "Phenomenology of Relativistic $3 \to 3$ Reaction Amplitudes within the Isobar Approximation," Eur. Phys. J. C **79**, 56 (2019), arXiv:1809.10523 [hep-ph].

[30] Juerg Gasser and Akaki Rusetsky, "Solving integral equations in $\eta \to 3\pi$," Eur. Phys. J. C **78**, 906 (2018), arXiv:1809.06399 [hep-ph].

[31] M. Albaladejo, D. Winney, I. V. Danilkin, C. Fernández-Ramírez, V. Mathieu, M. Mikhasenko, A. Pilloni, J. A. Silva-Castro, and A. P. Szczepaniak (JPAC), "Khuri-Treiman equations for 3π decays of particles with spin," Phys. Rev. D **101**, 054018 (2020), arXiv:1910.03107 [hep-ph].

[32] M. Mikhasenko *et al.* (JPAC), "Dalitz-plot decomposition for three-body decays," Phys. Rev. D **101**, 034033 (2020), arXiv:1910.04566 [hep-ph].

[33] M. Mikhasenko, Y. Wunderlich, A. Jackura, V. Mathieu, A. Pilloni, B. Ketzer, and A.P. Szczepaniak, "Three-body scattering: Ladders and Resonances," JHEP **08**, 080 (2019), arXiv:1904.11894 [hep-ph].

[34] A. Martinez Torres, K. P. Khemchandani, and E. Oset, "Three body resonances in two meson-one baryon systems," Phys. Rev. C **77**, 042203 (2008), arXiv:0706.2330 [nucl-th].

[35] P. C. Magalhaes, M. R. Robilotta, K. S. F. F. Guimaraes, T. Frederico, W. de Paula, I. Bediaga, A. C. dos Reis, C. M. Maekawa, and G. R. S. Zarnauskas, "Towards three-body unitarity in $D^+ \to K^-\pi^+\pi^+$," Phys. Rev. D **84**, 094001 (2011), arXiv:1105.5120 [hep-ph].

[36] A. Martinez Torres, K. P. Khemchandani, and E. Oset, "Solution to Faddeev equations with two-body experimental amplitudes as input and application to $J^P = 1/2^+$, $S = 0$ baryon resonances," Phys. Rev. C **79**, 065207 (2009), arXiv:0812.2235 [nucl-th].

[37] A. Martinez Torres, K. P. Khemchandani, D. Jido, and A. Hosaka, "Theoretical support for the $\pi(1300)$ and the recently claimed $f_0(1790)$ as molecular resonances," Phys. Rev. D **84**, 074027 (2011), arXiv:1106.6101 [nucl-th].

[38] R. T. Aoude, P. C. Magalhães, A. C. Dos Reis, and M. R. Robilotta, "Multimeson model for the $D^+ \to K^+K^-K^+$ decay amplitude," Phys. Rev. D **98**, 056021 (2018), arXiv:1805.11764 [hep-ph].

[39] Ian J. R. Aitchison, "Unitarity, Analyticity and Crossing Symmetry in Two- and Three-hadron Final State Interactions," (2015), arXiv:1507.02697 [hep-ph].

[40] I. J. R. Aitchison and R. Pasquier, "Three-Body Unitarity and Khuri-Treiman Amplitudes," Phys. Rev. 152, 1274 (1966).

[41] M. Mai, B. Hu, M. Döring, A. Pilloni, and A. Szczepaniak, "Three-body Unitarity with Isobars Revisited," Eur. Phys. J. A 53, 177 (2017), arXiv:1706.06118 [nucl-th].

[42] R. Aaron, R. D. Amado, and J. E. Young, "Relativistic three-body theory with applications to $\pi - N$ scattering," Phys. Rev. 174, 2022–2032 (1968).

[43] R. Aaron and R. D. Amado, "Analysis of three-hadron final states," Phys. Rev. Lett. 31, 1157–1159 (1973).

[44] Sebastian M. Dawid and Adam P. Szczepaniak, "Bound states in the B-matrix formalism for the three-body scattering," Phys. Rev. D 103, 014009 (2021), arXiv:2010.08084 [nucl-th].

[45] Xu Zhang, Christoph Hanhart, Ulf-G. Meißner, and Ju-Jun Xie, "Remarks on non-perturbative three–body dynamics and its application to the $KK\bar{K}$ system," (2021), arXiv:2107.03168 [hep-ph].

[46] Daniel Sadasivan, Maxim Mai, Hakan Akdag, and Michael Döring, "Dalitz plots and lineshape of $a_1(1260)$ from a relativistic three-body unitary approach," Phys. Rev. D 101, 094018 (2020), arXiv:2002.12431 [nucl-th].

[47] S. Schael et al. (ALEPH), "Branching ratios and spectral functions of tau decays: Final ALEPH measurements and physics implications," Phys. Rept. 421, 191–284 (2005), arXiv:hep-ex/0506072.

[48] R. Molina, M. Döring, W. H. Liang, and E. Oset, "The $\pi f_0(500)$ decay of the $a_1(1260)$," (2021), arXiv:2107.07439 [hep-ph].

[49] G. Janssen, J. W. Durso, K. Holinde, B. C. Pearce, and J. Speth, "$\pi\rho$ scattering and the πNN form-factor," Phys. Rev. Lett. 71, 1978–1981 (1993).

[50] M. F. M. Lutz and E. E. Kolomeitsev, "On meson resonances and chiral symmetry," Nucl. Phys. A 730, 392–416 (2004), arXiv:nucl-th/0307039.

[51] L. Roca, E. Oset, and J. Singh, "Low lying axial-vector mesons as dynamically generated resonances," Phys. Rev. D 72, 014002 (2005), arXiv:hep-ph/0503273.

[52] L. S. Geng, E. Oset, L. Roca, and J. A. Oller, "Clues for the existence of two $K_1(1270)$ resonances," Phys. Rev. D 75, 014017 (2007), arXiv:hep-ph/0610217.

[53] Markus Wagner and Stefan Leupold, "Tau decay and the structure of the a_1," Phys. Lett. B 670, 22–26 (2008), arXiv:0708.2223 [hep-ph].

[54] Markus Wagner and Stefan Leupold, "Information on the structure of the a_1 from tau decay," Phys. Rev. D 78, 053001 (2008), arXiv:0801.0814 [hep-ph].

[55] M. F. M. Lutz and S. Leupold, "On the radiative decays of light vector and axial-vector mesons," Nucl. Phys. A 813, 96–170 (2008), arXiv:0801.3821 [nucl-th].

[56] H. Kamano, S. X. Nakamura, T. S. H. Lee, and T. Sato, "Unitary coupled-channels model for three-mesons decays of heavy mesons," Phys. Rev. D 84, 114019 (2011), arXiv:1106.4523 [hep-ph].

[57] H. Nagahiro, K. Nawa, S. Ozaki, D. Jido, and A. Hosaka, "Composite and elementary natures of $a_1(1260)$ meson," Phys. Rev. D 83, 111504 (2011), arXiv:1101.3623 [hep-ph].

[58] Yu Zhou, Xiu-Lei Ren, Hua-Xing Chen, and Li-Sheng Geng, "Pseudoscalar meson and vector meson interactions and dynamically generated axial-vector mesons," Phys. Rev. D 90, 014020 (2014), arXiv:1404.6847 [nucl-th].

[59] Xu Zhang and Ju-Jun Xie, "The three-pion decays of the $a_1(1260)$," Commun. Theor. Phys. 70, 060 (2018), arXiv:1712.05572 [nucl-th].

[60] M. Mikhasenko, A. Pilloni, M. Albaladejo, C. Fernández-Ramírez, A. Jackura, V. Mathieu, J. Nys, A. Rodas, B. Ketzer, and A. P. Szczepaniak (JPAC), "Pole position of the $a_1(1260)$ from τ-decay," Phys. Rev. D 98, 096021 (2018), arXiv:1810.00016 [hep-ph].

[61] L. R. Dai, L. Roca, and E. Oset, "Tau decay into ν_τ and $a_1(1260)$, $b_1(1235)$, and two $K_1(1270)$," Eur. Phys. J. C 80, 673 (2020), arXiv:2005.02653 [hep-ph].

[62] J. M. Dias, G. Toledo, L. Roca, and E. Oset, "Unveiling the K1(1270) double-pole structure in the $B^- \to J/\psi\rho K^-$ and $B^- \to J/\psi K^{-*}\pi$ decays," Phys. Rev. D 103, 116019 (2021), arXiv:2102.08402 [hep-ph].

[63] M. G. Bowler, "The A1 Revisited," Phys. Lett. B 182, 400–404 (1986).

[64] Johann H. Kuhn and E. Mirkes, "Structure functions in tau decays," Z. Phys. C 56, 661–672 (1992), [Erratum: Z.Phys.C 67, 364 (1995)].

[65] Nathan Isgur, Colin Morningstar, and Cathy Reader, "The a1 in tau Decay," Phys. Rev. D 39, 1357 (1989).

[66] D. Gomez Dumm, P. Roig, A. Pich, and J. Portoles, "$\tau \to \pi\pi\pi\nu_\tau$ decays and the $a_1(1260)$ off-shell width revisited," Phys. Lett. B 685, 158–164 (2010), arXiv:0911.4436 [hep-ph].

[67] I. M. Nugent, T. Przedzinski, P. Roig, O. Shekhovtsova, and Z. Was, "Resonance chiral Lagrangian currents and experimental data for $\tau^- \to \pi^-\pi^-\pi^+\nu_\tau$," Phys. Rev. D 88, 093012 (2013), arXiv:1310.1053 [hep-ph].

[68] L. R. Dai, L. Roca, and E. Oset, "τ decay into a pseudoscalar and an axial-vector meson," Phys. Rev. D 99, 096003 (2019), arXiv:1811.06875 [hep-ph].

[69] C. B. Lang, Luka Leskovec, Daniel Mohler, and Sasa Prelovsek, "Axial resonances a$_1$(1260), b$_1$(1235) and their decays from the lattice," JHEP 04, 162 (2014), arXiv:1401.2088 [hep-lat].

[70] M. Mai and M. Döring, "Three-body Unitarity in the Finite Volume," Eur. Phys. J. A53, 240 (2017), arXiv:1709.08222 [hep-lat].

[71] Maxim Mai and Michael Döring, "Finite-Volume Spectrum of $\pi^+\pi^+$ and $\pi^+\pi^+\pi^+$ Systems," Phys. Rev. Lett. 122, 062503 (2019), arXiv:1807.04746 [hep-lat].

[72] Maxim Mai, Andrei Alexandru, Ruairí Brett, Chris Culver, Michael Döring, Frank X. Lee, and Daniel Sadasivan, "Three-body dynamics of the $a_1(1260)$ resonance from lattice QCD," (2021), arXiv:2107.03973 [hep-lat].

[73] Maxim Mai, Michael Döring, and Akaki Rusetsky, "Multi-particle systems on the lattice and chiral extrapolations: a brief review," Eur. Phys. J. Spec. Top. (2021), 10.1140/epjs/s11734-021-00146-5, arXiv:2103.00577 [hep-lat].

[74] Maxwell T. Hansen and Stephen R. Sharpe, "Lattice QCD and Three-particle Decays of Resonances," Ann. Rev. Nucl. Part. Sci. 69, 65–107 (2019), arXiv:1901.00483 [hep-lat].

[75] Akaki Rusetsky, "Three particles on the lattice," PoS LATTICE2019, 281 (2019), arXiv:1911.01253 [hep-lat].

[76] Joachim Kuhn *et al.* (E852), "Exotic meson production in the $f_1(1285)\pi^-$ system observed in the reaction $\pi^- p \to \eta\pi^+\pi^-\pi^- p$ at 18 GeV/c," Phys. Lett. B **595**, 109–117 (2004), arXiv:hep-ex/0401004.

[77] Paulo F. Bedaque and Harald W. Grießhammer, "Quartet S wave neutron deuteron scattering in effective field theory," Nucl. Phys. **A671**, 357–379 (2000), arXiv:nucl-th/9907077 [nucl-th].

[78] H. W. Hammer, J. Y. Pang, and A. Rusetsky, "Three particle quantization condition in a finite volume: 2. general formalism and the analysis of data," JHEP **10**, 115 (2017), arXiv:1707.02176 [hep-lat].

[79] Suh Urk Chung, "Spin formalism," (1971), 10.5170/CERN-1971-008.

[80] S. D. Protopopescu, M. Alston-Garnjost, A. Barbaro-Galtieri, Stanley M. Flatte, J. H. Friedman, T. A. Lasinski, G. R. Lynch, M. S. Rabin, and F. T. Solmitz, "$\pi\pi$ Partial Wave Analysis from Reactions $\pi^+ p \to \pi^+\pi^-\Delta^{++}$ and $\pi^+ p \to K^+ K^-\Delta^{++}$ at 7.1-GeV/c," Phys. Rev. **D7**, 1279 (1973).

[81] P. Estabrooks and Alan D. Martin, "$\pi\pi$ Phase Shift Analysis Below the $K\bar{K}$ Threshold," Nucl. Phys. **B79**, 301–316 (1974).

[82] Zhi-Hui Guo and J. A. Oller, "Resonances from meson-meson scattering in U(3) CHPT," Phys. Rev. D **84**, 034005 (2011), arXiv:1104.2849 [hep-ph].

[83] J. A. Oller, E. Oset, and J. R. Pelaez, "Meson meson interaction in a nonperturbative chiral approach," Phys. Rev. **D59**, 074001 (1999), [Erratum: Phys. Rev.D75,099903(2007)], arXiv:hep-ph/9804209 [hep-ph].

[84] M. Döring, C. Hanhart, F. Huang, S. Krewald, and U.-G. Meißner, "Analytic properties of the scattering amplitude and resonances parameters in a meson exchange model," Nucl. Phys. A **829**, 170–209 (2009), arXiv:0903.4337 [nucl-th].

[85] D. Rönchen, M. Döring, F. Huang, H. Haberzettl, J. Haidenbauer, C. Hanhart, S. Krewald, U.-G. Meißner, and K. Nakayama, "Coupled-channel dynamics in the reactions $\pi N \to \pi N$, ηN, $K\Lambda$, $K\Sigma$," Eur. Phys. J. A **49**, 44 (2013), arXiv:1211.6998 [nucl-th].

[86] D. Rönchen, M. Döring, F. Huang, H. Haberzettl, J. Haidenbauer, C. Hanhart, S. Krewald, U. G. Meißner, and K. Nakayama, "Photocouplings at the Pole from Pion Photoproduction," Eur. Phys. J. A **50**, 101 (2014), [Erratum: Eur.Phys.J.A 51, 63 (2015)], arXiv:1401.0634 [nucl-th].

[87] Maxim Mai, Michael Döring, Carlos Granados, Helmut Haberzettl, Ulf-G. Meißner, Deborah Rönchen, Igor Strakovsky, and Ron Workman (Jülich-Bonn-Washington), "Jülich-Bonn-Washington model for pion electroproduction multipoles," Phys. Rev. C **103**, 065204 (2021), arXiv:2104.07312 [nucl-th].

[88] N. Suzuki, T. Sato, and T. S. H. Lee, "Extraction of Electromagnetic Transition Form Factors for Nucleon Resonances within a Dynamical Coupled-Channels Model," Phys. Rev. C **82**, 045206 (2010), arXiv:1006.2196 [nucl-th].

[89] B. Julia-Diaz, H. Kamano, T. S. H. Lee, A. Matsuyama, T. Sato, and N. Suzuki, "Dynamical coupled-channels analysis of p(e,e-prime pi)N reactions," Phys. Rev. C **80**, 025207 (2009), arXiv:0904.1918 [nucl-th].

[90] H. Kamano, S. X. Nakamura, T. S. H. Lee, and T. Sato, "Nucleon resonances within a dynamical coupled-channels model of πN and γN reactions," Phys. Rev. C **88**, 035209 (2013), arXiv:1305.4351 [nucl-th].

[91] F. Huang, M. Döring, H. Haberzettl, J. Haidenbauer, C. Hanhart, S. Krewald, Ulf-G. Meißner, and K. Nakayama, "Pion photoproduction in a dynamical coupled-channels model," Phys. Rev. C **85**, 054003 (2012), arXiv:1110.3833 [nucl-th].

[92] D. Rönchen, M. Döring, and Ulf-G. Meißner, "The impact of $K^+\Lambda$ photoproduction on the resonance spectrum," Eur. Phys. J. A **54**, 110 (2018), arXiv:1801.10458 [nucl-th].

[93] Vladimir Gribov, *Strong Interactions of Hadrons at High Energies : Gribov Lectures on Theoretical Physics* (Cambridge University Press, Leiden, 2008).

[94] G. Janssen, K. Holinde, and J. Speth, "A Meson exchange model for pi rho scattering," Phys. Rev. C **49**, 2763–2776 (1994).

[95] Michael I. Haftel and Frank Tabakin, "Nuclear Saturation and smoothness of nucleon-nucleon potentials," Nucl. Phys. A **158**, 1–42 (1970).

[96] Michael Döring, Ulf-G. Meißner, and Wei Wang, "Chiral Dynamics and S-wave Contributions in Semileptonic B decays," JHEP **10**, 011 (2013), arXiv:1307.0947 [hep-ph].

[97] S. Ceci, M. Döring, C. Hanhart, S. Krewald, U.-G. Meißner, and A. Švarc, "Relevance of complex branch points for partial wave analysis," Phys. Rev. C **84**, 015205 (2011), arXiv:1104.3490 [nucl-th].

[98] Michel Davier, Andreas Höcker, Bogdan Malaescu, Chang-Zheng Yuan, and Zhiqing Zhang, "Update of the ALEPH non-strange spectral functions from hadronic τ decays," Eur. Phys. J. C **74**, 2803 (2014), arXiv:1312.1501 [hep-ex].

[99] "Invariant mass squared distributions from ALEPH," http://aleph.web.lal.in2p3.fr/tau/specfun13.html.

[100] Hiroyuki Kamano, "Electromagnetic N^* Transition Form Factors in the ANL-Osaka Dynamical Coupled-Channels Approach," Few Body Syst. **59**, 24 (2018).

[101] M. Döring, C. Hanhart, F. Huang, S. Krewald, U.-G. Meißner, and D. Rönchen, "The reaction $\pi^+ p \to K^+\Sigma^+$ in a unitary coupled-channels model," Nucl. Phys. A **851**, 58–98 (2011), arXiv:1009.3781 [nucl-th].

[102] Peter C. Bruns, Ludwig Greil, and Andreas Schäfer, "Chiral behavior of vector meson self energies," Phys. Rev. D **88**, 114503 (2013), arXiv:1309.3976 [hep-ph].

Appendix A: Technical details on spin-1 systems

For each helicity state $\lambda \in \{-1, 0, +1\}$ of the spin-1 field, the four-vector ε depends on the direction of the propagation [79] as

$$\varepsilon_0(\boldsymbol{p}) = \frac{1}{m_\rho} \begin{pmatrix} p \\ E_p^\rho \cos\phi_{\boldsymbol{p}} \sin\theta_{\boldsymbol{p}} \\ E_p^\rho \sin\phi_{\boldsymbol{p}} \sin\theta_{\boldsymbol{p}} \\ E_p^\rho \cos\theta_{\boldsymbol{p}} \end{pmatrix}, \qquad \text{(A1)}$$

$$\varepsilon_{\pm 1}(\boldsymbol{p}) = \frac{1}{\sqrt{2}} \begin{pmatrix} 0 \\ \mp \cos\theta_{\boldsymbol{p}} \cos\phi_{\boldsymbol{p}} + i \sin\phi_{\boldsymbol{p}} \\ \mp \cos\theta_{\boldsymbol{p}} \sin\phi_{\boldsymbol{p}} - i \cos\phi_{\boldsymbol{p}} \\ \pm \sin\theta_{\boldsymbol{p}} \end{pmatrix}, \qquad \text{(A2)}$$

where $E_p^\rho := \sqrt{m_\rho^2 + \boldsymbol{p}^2}$ and we chose $m_\rho = 6.44\, m_\pi$. On-shell, this fulfills required properties, such as the transversality, i.e. $p_\mu \varepsilon^\mu = 0$ exactly, see Ref. [79]. Away from the on-shell point one can generalize the above definitions using $m_\rho \to \sqrt{E_p^2 - p^2}$. However, as the difference between both versions does not lead to new singularities of the spin-1 propagator, perturbation theory is viable, allowing one to reabsorb it into the local terms [102].

Equation (16) requires the calculation of the helicity sum for the s-channel ρ propagation,

$$\sum_\lambda \epsilon_{\lambda,\mu}(\boldsymbol{p})\epsilon_{\lambda,\nu}^*(\boldsymbol{p}) = -g_{\mu\nu} + \frac{p_\mu p_\nu}{m_\rho^2}. \qquad \text{(A3)}$$

Appendix B: Data consistency tests

Rather than considering all data correlations from Ref. [98] in the covariance matrix for the calculation of χ^2 using Eq. (31), we include only nearest neighbor correlations. All other correlations are neglected because we find that no reasonably smooth curve can describe the data when they are included as shown in the following.

We fit the ALEPH data with a Legendre Polynomial expansion, $f(\sqrt{s}, x_i)$ given by

$$f(\sqrt{s}, x_i) = \sum_{i=0}^{n} x_i P_n\left(\frac{\sqrt{s} - \sqrt{s_0}}{\sqrt{s_0}}\right), \qquad \text{(B1)}$$

where $\sqrt{s_0} = 1$ GeV is chosen such that the argument is always in the interval $[-1, 1]$ and the x_i are fitted by minimizing the χ^2,

$$\chi^2 = (\vec{f}(x_i) - \vec{\mathcal{L}})^T \Sigma^{-1} (\vec{f}(x_i) - \vec{\mathcal{L}}), \qquad \text{(B2)}$$

where $\vec{f}$ is constructed from the data at $\sqrt{s_i}$, $(\vec{f})_j = f(\sqrt{s_j}, x_i)$. Similarly, the central values of the data are collected in the vector $\vec{\mathcal{L}}$. When we fit in the range 0.6 GeV $< \sqrt{s} <$ 1.5 GeV, with $n = 10$ including all correlations we find that the minimum χ^2 for the 63 data points is 127 ($\chi^2_{\text{dof}} = 2.43$) as Table IV shows. Increasing
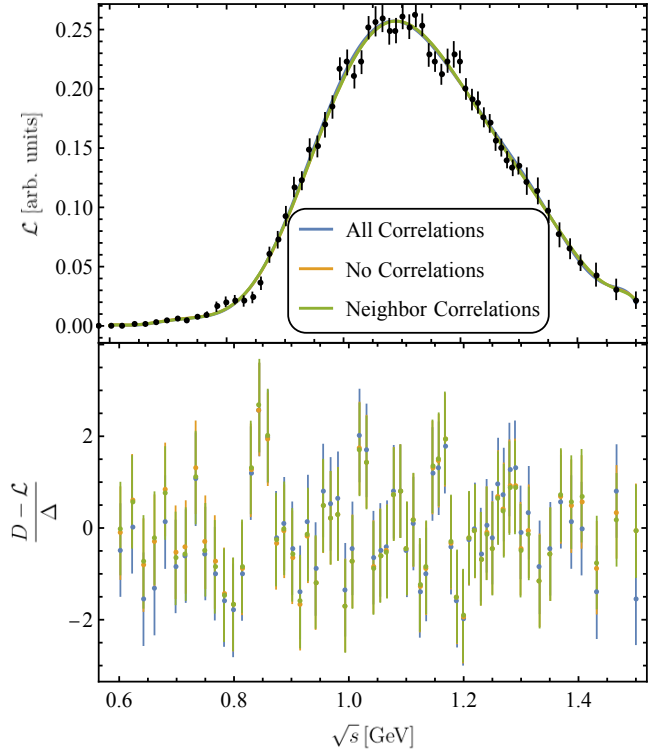

FIG. 13. The fits (upper row) and normalized residuals (lower row) using a Legendre Polynomial Expansion to the ALEPH data ($n = 10$ in Eq. (B1)). The color coding indicates the cases where the covariance matrix includes all correlations (blue), no correlations (orange), and nearest-neighbor correlations (green).

the number of polynomials in this expansion will decrease the total χ^2 but does not decrease the χ^2_{dof}. For example, when $n = 15$, $\chi^2 = 122$ and, therefore, $\chi^2_{\text{dof}} = 2.58$. We show the $n = 10$ fit and the residuals in Fig. 13. These results indicate that it is very difficult for any smooth curve, regardless of whether or not it is theoretically justified, to describe the data. In contrast, when we use the same function to perform a fit where we include only the uncorrelated uncertainties and set all correlations to 0, we find the total χ^2 for the 63 data points to be 62 indicating that the uncorrelated data can be easily fit with a smooth function. The orange line and data of Fig. 13 show the fit and residuals when none of the correlations are included in the data. This fit is quite similar to the one that includes all correlations even though the χ^2 is very different. We note that while this case demonstrates that the uncorrelated data can be reasonably described by a smooth function, the residuals still display some noticeable correlation. In order to account for these correlations we introduce another case, shown in blue in Fig. 13. Here, we include only the nearest-neighbor correlations. When we fit the data with $n = 10$ to this case, we obtain $\chi^2 = 64$. As this case includes the maximum of correlations that can be reconciled with a statistically sound description of the data, we regard this case as the data

	nearest neighbor correlations	no correlations	all correlations	all corr. (2005 data)
χ^2	64	62	127	16
No. data	63	63	63	75

TABLE IV. Total χ^2 for fits to the ALEPH data while various correlations were included. The first three entries refer to the 2013 data of Ref. [98] while the last column refers to the 2005 data of Ref. [47].
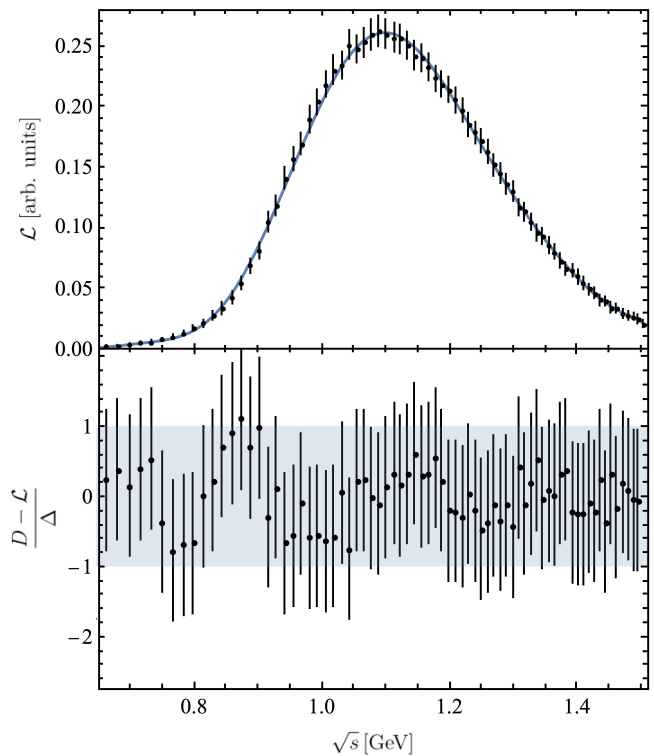

FIG. 14. Older ALEPH data [47], pertinent fit, and normalized fit residuals. These data are not used in the analysis. See Fig. 10 for notation.

set for the analysis described in the main text.

We also apply this phenomenological test to the data as they were originally published in Ref. [47]. These data, shown in Fig. 14, have since been updated in Ref. [98]. We find that the older data are considerably over-fit for $n = 10$ with a total χ^2 of 16 as shown in Table IV. We therefore discard these data.

In summary, all three fits shown in Fig. 13 are quite similar, even for the residuals. This implies that the best-fit parameters for each case will be quite similar regardless of which correlations are included. Thus, our choice of data (nearest-neighbor correlations only) affects the value of our χ^2, but it does not have much effect on the best values for pole position or residues.